WESLEYAN UNIVERSITY

RESONATOR DESIGN for the OBSERVATION of THIRD SOUND AMPLIFICATION by STIMULATED CONDENSATION (TASC)

by

Sergei Anatolievich Jerebets

A Thesis submitted to the Faculty
of Wesleyan University in partial fulfillment of
the requirements for the degree of Doctor of Philosophy

Middletown, Connecticut

May, 2002

Table of Contents

Chapter 1. Introduction

This chapter outlines the progress that has been made in the understanding of the unique nature of superfluid ^{4}He with an emphasis on two different theoretical descriptions of superfluidity. Third sound amplification by stimulated condensation (TASC) of helium vapor atoms into a resonating third sound mode is considered to be a logical consequence of peculiar properties of superfluid helium.

1.1 Liquid ^{4}He as quantum fluid

Fascinating properties of liquid helium become apparent right below 2.17 K, a temperature at wich an ordinary liquid helium, He I, under its saturated vapor pressure turns into a superfluid, He II, that flows without viscosity and transfers heat without a temperature gradient.

Superfluidity, since its discovery by Kapitza [1. 1], is considered to be a macroscopic manifestation of quantum effects controling helium atoms behavior [1. 2]. Introduced by London [1. 3], the first plausible microscopic explanation of superfluidity was based on Bose – Einstein condensation [1. 4, 1. 5] phenomenon. Extending this approach, Feynman [1. 6] argued that Bose-Einstein statistics determined all excitations in strongly interacting liquid ^{4}He except density fluctuations

in the vicinity of its ground state.

Landau [*1.7*] *had another picture of superfluidity in his mind when proposed He II excitation spectrum in which the excitations were quasiparticles. Moreover, he insisted that the phonon excitation spectrum itself was a sufficient condition for the superfluidity to occur in a system.*

Due to peculiar interactions between helium atoms, liquid helium shows its unique properties (*see Fig. 1. 1. 1 below*).

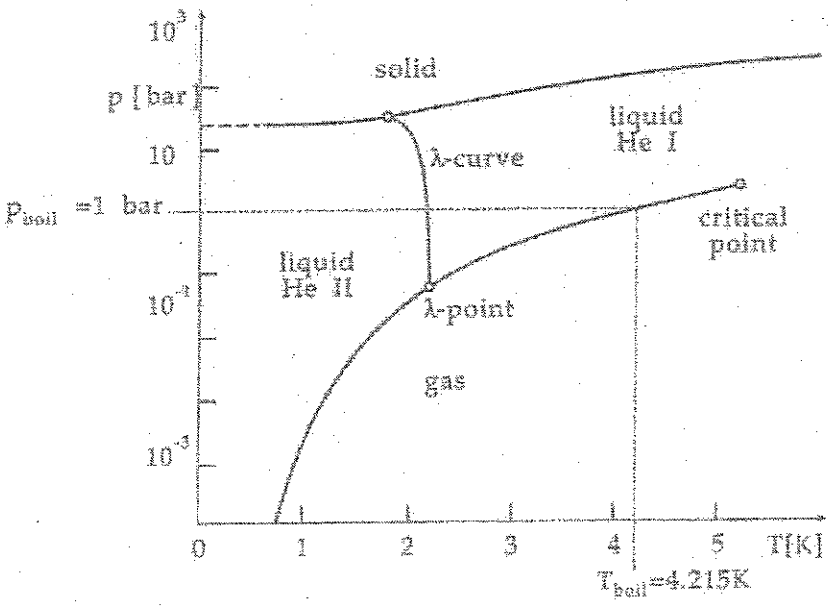

Figure 1. 1. 1. Phase diagram of ^{4}*He* (*after* [*1. 8*]).

Because the attractive part of the helium potential is weak [*1. 9*], *liquid* ^{4}*He is a weakly interacting system. Kinetic energy of localization, or zero − point energy,*

shifts the minimum of the total energy of the liquid phase to be lower than that of the solid. Therefore, the liquid phase remains stable around absolute zero and a solid phase does not appear unless a substantial external pressure is applied [*1. 10*]. *Due to a weak localization, the atomic wave functions of these both phases overlap and quantum statistics becomes a dominant factor in the description of condensed phases of helium.*

At the same time, liquid ^{4} *He is a strongly interacting system* [*1. 11*]. *Because of the symetry of helium atoms with their closed shell of two electrons, they experience a large hard core repulsive interaction.*

Thus, the dual nature of liquid helium has proved to be an extreme challenge for theoretical studies. Owing to its unique interplay of quantum effects, liquid helium is marked a quantum fluid [*1. 12*] *and represents the first physical system where the existence of Bose condensed phase is widely recognized* [*1. 13 – 1.15*].

Although the properties of the liquid helium cannot be treated as a simple perturbation of the ideal Bose gas, the latter is an instructive model to begin with to better understand the effects of Bose – Einstein condensation on liquid helium.

■ 1.2 The Bose – Einstein condensation

As a collection of non – interacting $\mathcal{N}$ particles in the volume $\mathcal{V}$, the ideal Bose gas (IBG) properties are entirely controlled by the Bose – Einstein statistics. The eigenstates of a single particle in a box are plane wave states with well – defined momentum $\mathbb{p}$. In the case of the IBG, these states are also the eigenstates of the many particle system. The statistical description of the particles in the box [1. 16] consists of specifying the number of particles occupying each of the single – particle eigenstates. This function is a single – particle momentum distribution $n_{\mathbb{p}}$ that specifies the number of particles in a state with momentum $\mathbb{p}$.

The particles in the gas are usually characterized by their thermal de Broglie wavelength given by

$$\lambda_{th} = \frac{\hbar}{\sqrt{2\,\pi\, m_4\, k_b\, T}}, \qquad (1.\,2.\,1)$$

where m_4 is a particle's mass, Boltzman's, $\kappa_b = 1.38 \times 10^{-23}\, J/K$ and Plank's, $\hbar = 6.63 \times 10^{-34}\, J\,sec$ constants, respectively, and T is a temperature.

When de Broglie wavelenth is much smaller than the average interparticle separation, $\lambda_{th} << (\mathcal{V}/\mathcal{N})^{1/3}$, particles are ruled by classical physics. The properties of the IBG at high temperatures are dominated by the thermal motion of the particles.

The momenta of the particles will be distributed according to the classical Maxwell – Boltzman distribution.

As a result of the particle wavefunction overlap, quantum effects become dominant when λ_{th} is large compared to the interparticle spacing, $\lambda_{th} >> (\mathcal{V}/\mathcal{N})^{1/3}$. By lowering the temperature further, λ_{th} of the particles begin to approach the interparticle spacing and n_p due to the appearence of quantum effects deviates from its classical Gaussian shape more and more. Having no restrictions, the occupation of states with small p gradually increases to reduce the energy of the system and a transition to the Bose – Einstein phase eventually happens [1. 17] when

$$\lambda_{th}^3 \mathcal{N}/\mathcal{V} = \zeta(3/2) = 2.612, \qquad (1.2.2)$$

where ζ is the Rieman zeta function. Transition temperature, T_C, is determined by

$$T_C = \frac{2\pi\hbar^2}{m_4 k_b}\left(\frac{\rho}{2.612}\right)^{2/3}, \qquad (1.2.3)$$

where ρ is gas density. Around T_C, the occupancy of any particular single – particle momentum state remains finite and the number of particles in the excited states, $\mathcal{N}_\epsilon$, is given by $\mathcal{N}_\epsilon = \mathcal{N}(T/T_C)^{3/2}$. Below T_C, a macroscopic occupation of the zero momentum state develops (Fig. 1. 2. 1) :

$$n_o \equiv \mathcal{N}_0 = \mathcal{N} - \mathcal{N}_\epsilon = \mathcal{N}\left[1 - (T/T_c)^{3/2}\right], \qquad (1.2.4)$$

which signals the phenomenon of Bose – Einstein condensation.

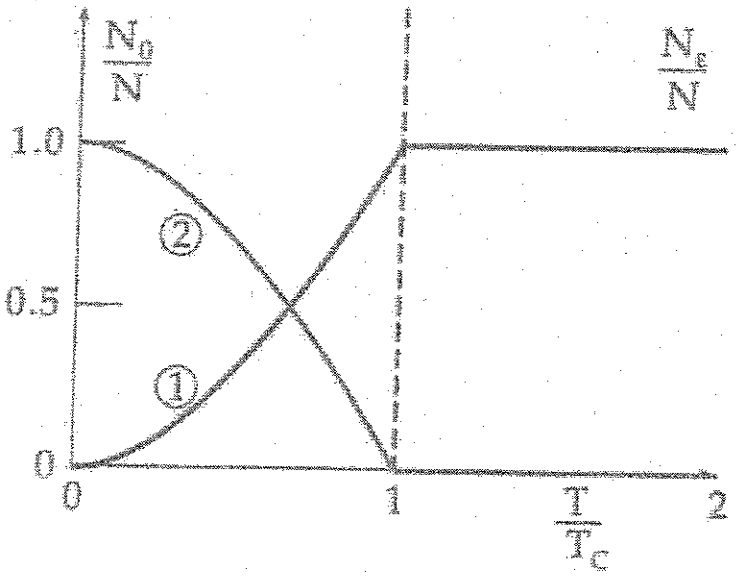

Figure 1.2.1. Temperature variations of $\mathcal{N}_0/\mathcal{N}$ and $\mathcal{N}_\epsilon/\mathcal{N}$ for IBG (after [1.8]).

This condensation is reflected in n_p by the appearence of the Kronecker delta δ_{op} component with a weight determined by the condensate fraction n_o [1.18]

$$n_p = n_o\,\delta_{op} + n_p^{a} \qquad (1.2.5)$$

and a term n_p^{a} contributed by the uncondensed atoms momentum distribution.

At $T = 0\,K$, the condensate component contains all of the intensity meaning that every particle in the system is in the ground zero energy state.

To see how the IBG system relates to helium, let us estimate the condensation temperature for gaseous ^{4}He. If in equation (1. 2. 3) we use the particle density ρ appropriate to the saturated vapour at the normal boiling point, we find $T_C = 0.5\,K$. Since the boiling point is 4.2 K, the Bose – Einstein condensation is not observed in a gas. However, if we use the density of liquid ^{4}He instead, we obtain $T_C = 3.13\,K$, which is close to $T_\lambda = 2.17\,K$, the temperature of the λ – transition (see Fig. 1. 1. 1).

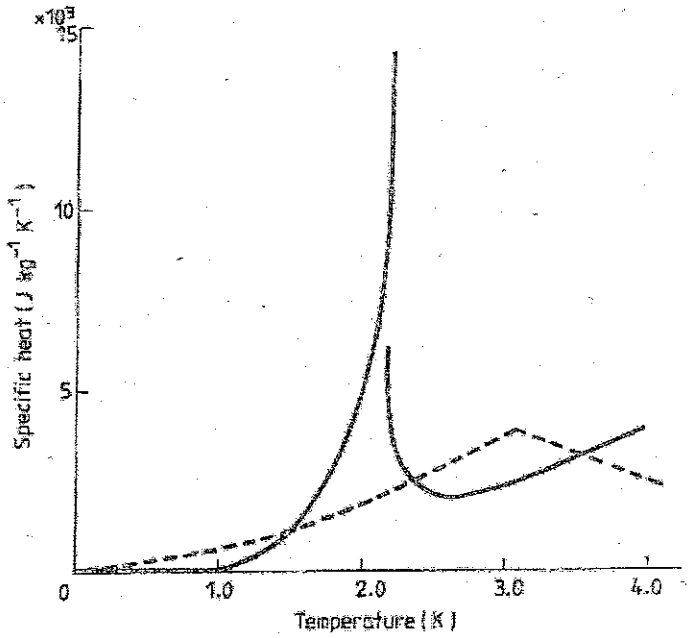

Figure 1. 2. 2. Specific heat of liquid ^{4}He [1. 20]. Broken line shows specific heat of IBG having the same density as liquid ^{4}He (after [1. 19]).

There is a qualitative correspondence between the temperature variations (Fig. 1. 2. 1) of $\mathcal{N}_0(T)$ *and* $\mathcal{N}_\epsilon(T)$ *and those (Fig. 1. 3. 1, see below) of* ρ_s/ρ *and* ρ_n/ρ, *respectively, as well. These similarities are sufficient to suggest [1. 19] that* T_λ *marks the onset of Bose – Einstein condensation in liquid* ^{4} *He. On the other hand, the specific heat anomalies in the two cases are quite different (see Fig. 1. 2. 2 above), the IBG showing a cusp singularity in* C_v *as opposed to the* λ *discontinuity of liquid* ^{4} *He.*

Since liquid helium is interacting fluid, it is not surprising that the IBG model does not give an accurate description of the λ *transition. Due to the interactions, the number of particles condensed into the lowest energy level is reduced, and the nature of the excited levels of the system is altered. At absolute zero, not all the particles are in the lowest single particle energy level, but some are raised to the levels of slightly higher energy. It means that the condensate is depleted (Fig. 1. 2. 3) by the interactions [1. 19]. An important point is that the lowest level is still macroscopically populated, and this remains true up to a finite condensation temperature. At temperatures above zero, partially populated thermally excited levels of the system no longer correspond to single – particle states, but to the elementary excitations of the whole system.*

Measurements of n_p *for superfluid* ^{4} *He in high – momentum transfer neutron scattering experiments [1. 15] allowed to estimate condensate fraction* n_0 *(Fig. 1. 2. 3) :*

$$n_0(T) = n_0(0)\,[1 - (T/T_\lambda)^\alpha] \qquad (1.2.6)$$

Experimental results determine $n_0(0) = (13.9 \pm 2.3)\,\%$ *which is to be compared with*

theoretical (✱) values (Fig. 1. 2. 3) of 9 % [1. 23] and 11.3 % [1. 24] for $\alpha = 3.6 \pm 1.4$.

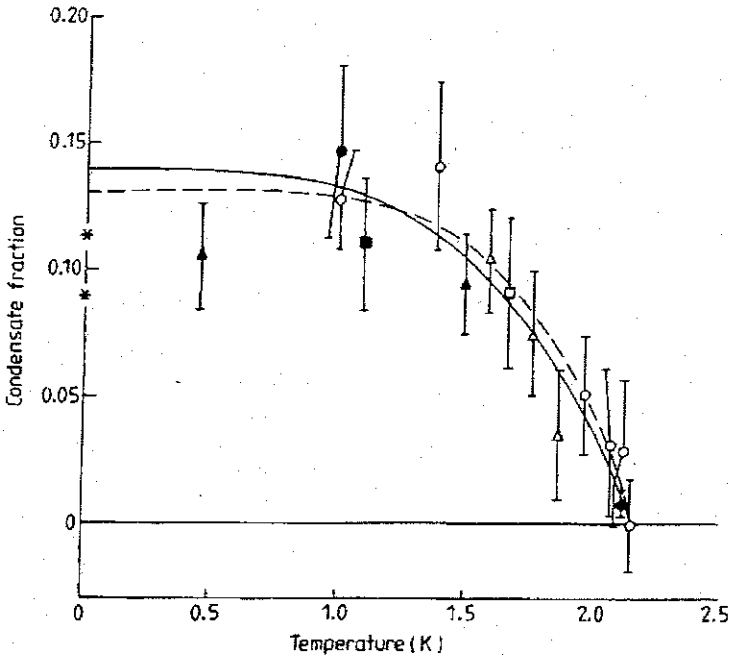

Figure 1. 2. 3. Condensate fraction in superfluid ^{4} *He (after [1. 19]). Results from momentum distribution* n_p *: ● and ■ are from [1. 15]. Results from pair – correlation function : □ from X – ray scattering [1. 15]; ○ and △ – from neutron scattering [1. 13, 1. 15]. Solid line is least squares fit of equation (1. 2. 6) to these data [1. 15]. ▲ – later results [1. 21]. Broken curve is surface tension calculated data [1. 22].*

The experimental evidence (Fig. 1. 1. 1) of He II superfluidity at absolute zero permited Landau [1. 7] to build the description of an interacting Bose system using a quite different physicsl picture, the famous two – fluid model.

1.3 The two – fluid model

Landau developed [1. 25] quantum hydrodynamics and introduced his criterion of superfluidity linking the latter to the He II excitation spectrum. There was no analogy with Bose – Einstein condensation because IBG could not be considered as superfluid. At absolute zero, He II fluid is in its ground state and consists only of the superfluid ($\rho = \rho_S$), a single quantum state having no entropy ($\mathcal{S}_S = 0$) and viscosity. The flow of mass is ρv_S. As temperature is increased, thermal excitations are created in the fluid and these excitations carry the entropy of the fluid. Landau [1. 7] proposed two types of excitations : phonons and rotons. The first was a collective density sound excitation with a linear phonon dispersion relation at low momentum. The second was a macroscopic rotation of the fluid which he reffered to as a vortex motion. These excitations comprise a normal fluid that has a velocity ($v_n - v_S$) relative to the ground state. They contribute an amount $\rho_n (v_n - v_S)$ to the mass current, where ρ_n is a normal fluid density which converts velocity to mass current. The total mass current j is given by [1. 18] to be

$$j = \rho v_S + \rho_n (v_n - v_S) = (\rho - \rho_n) v_S + \rho_n v_n = \rho_S v_S + \rho_n v_n, \qquad (1.3.1)$$

where density of superfluid $\rho_S = \rho - \rho_n$. In this formulation ρ_S is a derived quantity and $\rho_n (T) / \rho$ (Fig. 1. 3. 1) is determined by the number of excitations at temperature T [1. 26] and was measured [1. 27] to validate the two – fluid model predictions.

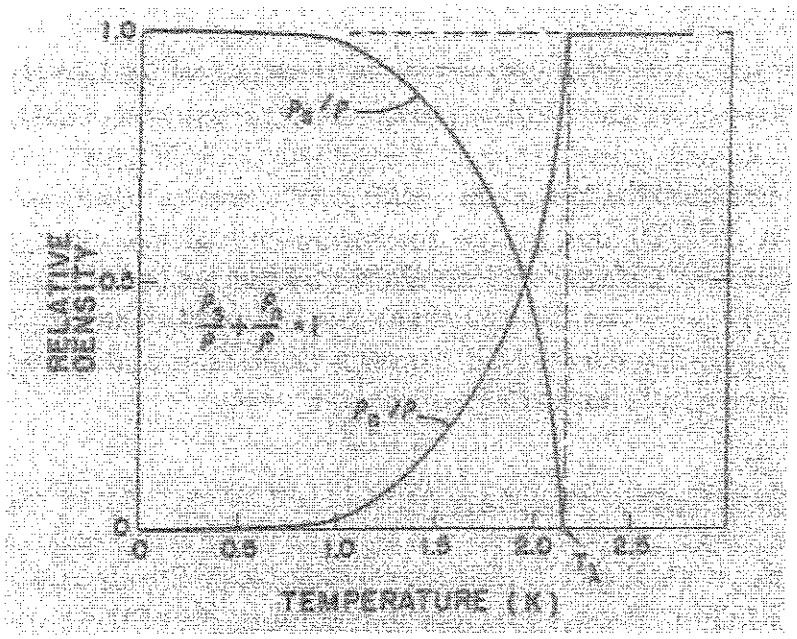

Figure 1. 3. 1. The superfluid, ρ_S and normal fluid, ρ_n densities from a torsional pendulum experiment [*1. 27*] (*after* [*1. 18*]).

The concept of elementary excitations was successfully applied to explain the specific heat (*Fig. 1. 2.2*) *and thermodynamic properties of He II. To have a better correspondence with experimental data* [*1. 28*], *Landau revised* [*1. 29*] *his phonon - roton excitation spectrum which now is in excellent agreement with neutron scattering* [*1. 30*] *experiments* (*see Fig. 1. 3. 2 below*).

In analogy to classical hydrodynamics, irrotational superfluid velocity field [*1. 7*] *was also introduced for He II undergoing potential flow*

$$\nabla \times v_S = 0 \qquad (1.3.2)$$

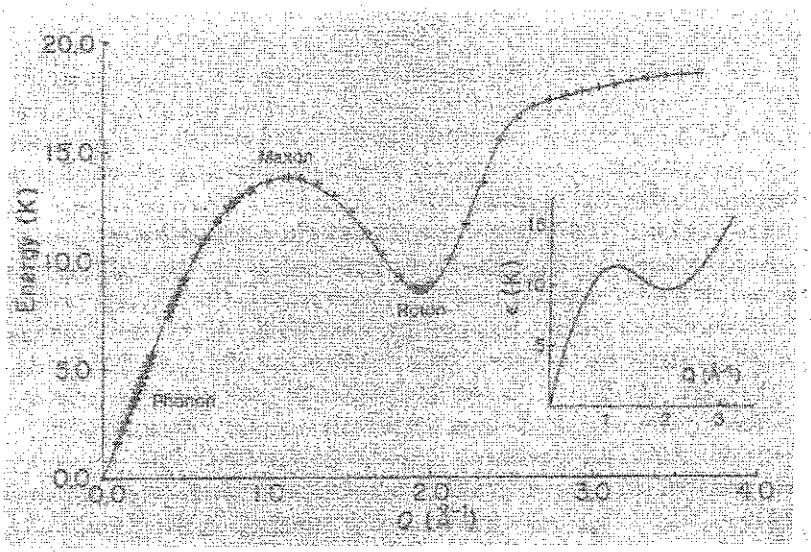

Figure 1. 3. 2. The phonon – roton energy (after [1. 18]) compiled from several neutron scattering measurements [1. 30]. The inset shows Landau spectrum [1. 29].

as well as a phenomenological equation of motion for the superfluid

$$m_4 \frac{\partial v_s}{\partial t} = -\nabla\left(\mu + m_4 {v_s}^2/2\right) \qquad (1.3.3)$$

with potential energy per particle, μ. Equation (1. 3. 3) describes non – dissipative potential flow and provides a basis for our understanding of superfluidity. As it appears, equation (1. 3. 3) can also be derived using a condensate wave function which implies that superfluidity can effectively be treated as quantum phenomenon as well.

▪ 1.4 Wave function of the condensate

London [1. 31] treated superfluids as systems condensed into a single quantum state and introduced a macroscopic wave function of coherent phase to describe a condensate at absolute zero.

$$\Psi_{BEC}(r,\ t) = \Psi_o(r,\ t)\, e^{i\varphi(r,t)}, \qquad (1.4.1)$$

where the phase $\varphi(r,\ t)$ is a real function of position r nd time t [1. 19]. Normalization is chosen to accomodate the fact that (1. 4. 1) is a macroscopic wave function and (1. 4. 2) is equal to the average number of superfluid atoms in unit volume.

$$\Psi^*_{BEC}(r,\ t)\, \Psi_{BEC}(r,\ t) = \Psi_o{}^2(r,\ t) = \rho_S / m_4 \qquad (1.4.2)$$

From the definition of quantum momentum : $\hat{p}\,\Psi = -i\hbar\,\nabla\Psi = p\ \Psi$ for the He II case, we obtain a velocity of the superfluid

$$v_S = \frac{\hbar}{m_4}\,\nabla\varphi \qquad (1.4.3)$$

to be proportional to the gradient of the condensate wave function phase $\varphi(r,\ t)$.

We notice from equation (1. 4. 3) that when the superfluid is at rest, the phase

has the same value throughout; when the superfluid velocity is finite and constant, the phase varies uniformly in the direction of v_s. *It means that the phase of the wave function (1. 4. 1) is coherent for the whole superfluid [1. 19], moreover,* $\varphi(r, t)$ *is slowly varying function even on a macroscopic scale. The effect of phase coherence is to lock the condensate atoms together in momentum space in a state of uniform motion.*

Making use of conjugate variables $\mathcal{N}$ *and* $\hbar\varphi$ *with the Hamiltonian* $\mathcal{H}$ *that included the kinetic energy of the superfluid and the energy of the whole fluid at rest, Anderson [1. 32] suggested an elegant derivation of Landau's equation of motion (1. 3. 3) for the superfluid [1. 19]*

$$\hbar \frac{\partial \varphi}{\partial t} = -\frac{\partial \mathcal{H}}{\partial \mathcal{N}} = -\left(\mu + m_4 v_s^2 / 2\right) \qquad (1.4.4)$$

which supported the idea of phase coherence and had a profound impact later on in the understanding of Josephson effects [1. 32 – 1. 34].

Keeping in mind Landau spectrum for the superfluid (Fig. 1. 3. 2), we might write down the wave function of the superfluid at finite temperatures as shown

$$\Psi_{T\neq 0}(r, t) = \Psi_{BEC}(r, t) + \sum_n C_n \phi_n, \qquad (1.4.5)$$

where summation in (1. 4. 5) accounts for the presence of the excitations. As $T \to 0$, *the system ends up in the ground state described by (1. 4. 1) and will remain there.*

1.5 TASC idea

Described by the wave function (1. 4. 5), a macroscopic quantum state of superfluid He II will be insensitive to microscopic events as long as the equilibrium conditions are maintained. The condensation of vapor atoms into a moving super-current is a remarkable example of its persistence [1. 35]. Both kinetic energy and angular momentum of a rotating superfluid will increase along with the total mass of the superfluid when vapor atoms enter the film.

A resonating third sound mode will be occupied by a macroscopically large number of particles in a state into which condensing vapor atoms will coherently join. Because a local flow field of the third sound on the microscopic time and size scales of the condensation event appears to be no different than that of persistent current, the condensing vapor atoms will be accommodated into local, instantaneous velocity field of the third sound wave.

An additional feature that distinguishes the third sound from the persistent current lies in the acoustic nature of the former which reveals itself in a separation of energy and angular momentum of the particles constituting the medium. Therefore, superfluid mass can be removed from the third sound mode of definite angular momentum while preserving kinetic energy deposited by the coherent condensation.

It means that a continuous process of third sound amplification by stimulated condensation (TASC) of vapor atoms into the superfluid film is possible and this thesis presents an implemented design of the novel resonator to detect this

effect as well as necessary requirements to observe this phenomenon along with the first experimental results on the third sound obtained with the proposed resonator.

Chapter 2. TASC

Important similarities between a persistent current and third sound flow field phase structures can manifest themselves in the process of quantum condensation. Details of third sound amplification and necessary resonator requirements for its observation are discussed in this chapter as well.

2.1 Third sound modes in superfluid ^{4}He film

Depending on the experimental conditions, the various kinds of sound modes can be acommodated in He II. In bulk helium, density fluctuations propagate as first sound and temperature fluctuations as second sound [2. 1]. *The former occurs with the normal and superfluid components moving in phase under adiabatic conditions. The latter is observed when these two components are out of phase while the total density remains constant.*

Helium atoms adsorbed on a substrate constitute the film. By definition, third sound is a surface wave on a He II film (Fig. 2. 1. 1), *in which the superfluid oscillates parallel to the substrate, while the normal fluid is clamped because of its viscosity.*

Since the superfluid carries no entropy, the accumulation of superfluid at a wave crest lowers the temperature there, whereas near a trough temperature is raised due to a smaller superfluid fraction than in equilibrium (Fig. 2. 1. 1)

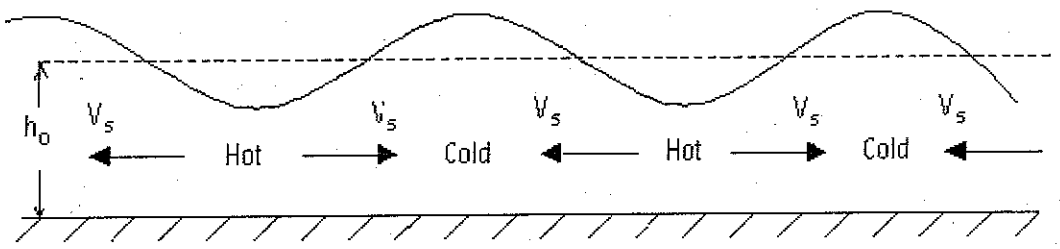

Figure 2. 1. 1. Third sound wave on He II film (after [1. 20]).

As a result, third sound wave is accompanied by the temperature fluctuations [2. 2].

In the limit of very long wavelengths compared to the film thickness h_o, the phase velocity c_3 of third sound by analogy with a shallow water wave [2. 3] case is

$$c_3 = \sqrt{g\, h_o}, \qquad (2.\ 1.\ 1)$$

where the main restoring force g – is the van der Waals force (per unit mass) of attraction between the helium atoms at the surface and the substrate where the film is.

For more than a decade third sound has been a valuable probe of superfluid film in our lab on a circular geometry resonator that determines shape of third sound mode. To find the latter, we combine a continuity equation for superfluid in the form

$$\frac{\partial h}{\partial t} = -h_o\, \nabla \cdot v_s \qquad (2.\ 1.\ 2)$$

with a linearized equation (1. 3. 3)

$$\frac{\partial v_S}{\partial t} = -g \nabla h \qquad (2.1.3)$$

and get a wave equation (2. 1. 4) for the film

$$\nabla^2 h - \frac{1}{c_3^2} \frac{\partial^2 h}{\partial t^2} = 0 \qquad (2.1.4)$$

which has a general solution : $h(r, \varphi, t) = h_0 + \eta(r, \varphi, t)$. *Here* h_0 *is the static thickness of the film (Fig. 2. 1. 1) and* $\eta(r, \varphi, t)$ *is the time dependent amplitude of the film oscillations that is represented in cylindrical coordinates* (r, φ) *by the Bessel functions* J_m *of the first kind* [2. 4].

$$\eta(r, \varphi, t) = \sum_{m,n} \eta_0 J_m(k_{mn} r) e^{i(m\varphi - \omega_{mn} t)} \qquad (2.1.5)$$

In equation (2. 1. 5) the angular frequency ω_{mn} *of the mode*

$$\omega_{mn} = c_3 k_{mn} = c_3 x_{mn} / a \qquad (2.1.6)$$

is determined by the speed c_3 *of third sound, the radius* a *of our resonator disk and values* x_{mn} *given by the* n *- th zero of* $J_m'(x_{mn})$, *"free" boundary condition at* $r = a$.

In practice (Chapter 4), we excite a third sound wave electrostatically by applying AC voltage to the drive electrodes and monitor the capacitance modulation of the pick − ups. Both drives and pick − ups are the parts of our detection system. Changes in capacitance are than converted to the amplitude of the film oscillations. By varying the drive frequency f_D, third sound resonance for a particular mode (Fig. 2. 1. 2)

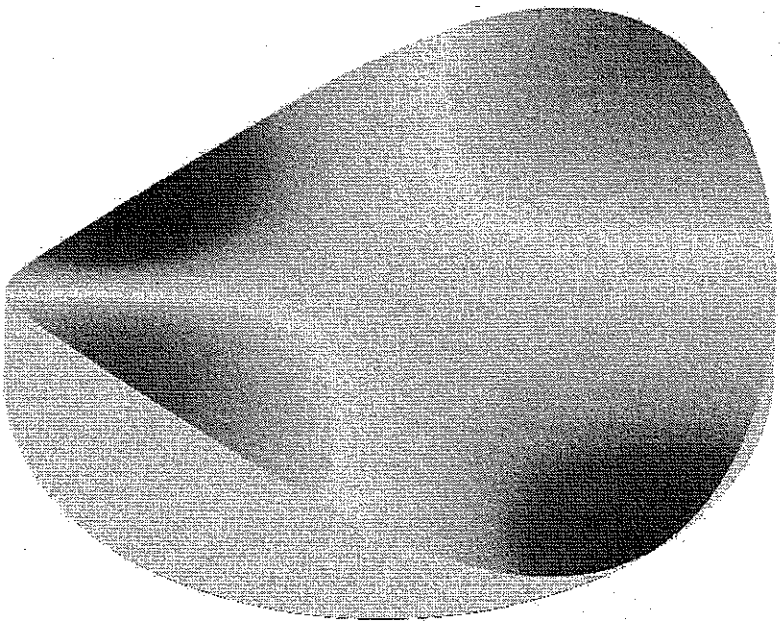

Figure 2. 1. 2. Third sound (2, 1) mode.

can be found at a resonance frequency $f_0 = c_3 \varkappa_{mn} / (4 \pi a)$. This allows us to get the third sound speed c_3 and infer the film thickness h_0 from a more accurate expression (2. 1. 7) for the third sound speed [2. 5], eventually.

$$c_3^2(h_0) = \frac{h_0 - D}{h_0} \frac{3 k_b T_V}{m_4 h_0^3} \qquad (2.1.7)$$

The strength of the Van der Waals potential, $T_V = 41\ K$, has been determined from the previous experiments [2. 5] as well as the healing length, $D = 0.526\ nm$ [2. 6].

Only the lowest (m, n) modes of well defined non − zero angular momentum and referenced by the number m of angular node lines and number n of radial antinodes had a practical interest for us. Special attention has been given to the (2, 1) third sound mode (Fig. 2. 1. 2) as our calculations and resonator design (Chapter 3) showed to be the most promising for the TASC effect.

■ 2.2 Persistent current and third sound phase structures

The most convincing experimental manifestation of superfluidity is the observation of persistent current in He II. Like a current in a closed loop superconducting wire, superfluid can be set into the motion and will remain in apparently the same flow state without a noticeable decay with time. A simple configuration in which persistent current can be created with a superfluid helium film adsorbed on the surface of the ring is shown in Fig. 2. 2. 1.

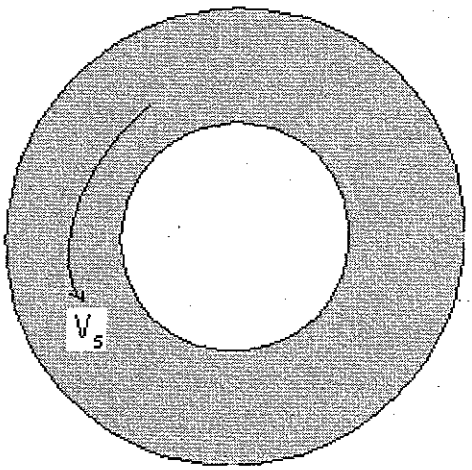

Figure 2. 2. 1. Quantised circulation of superfluid He II.

To find the flow pattern, we use formula (1. 4. 3) for the velocity v_S of the superfluid to calculate the circulation round any contour ℓ within the liquid.

$$\oint v_S \cdot d\ell = \frac{\hbar}{m_4} (\Delta\varphi)_\ell = \frac{n\,h}{m_4} \qquad (2.\,2.\,1)$$

Since the superfluid wave function is single – valued, a trip round a closed contour must leave it unchanged, with the result that the change in phase can be only an integral multiple of 2π *or zero. From equation* (2. 2. 1) *we see that the circulation is quantized in units of* h / m_4 *where* n *is an integer.*

Therefore, we can characterize persistent current by a static wavefunction phase $\varphi(r)$ *that varies in space perpendicular to the streamlines of the fluid flow and quantizes the velocity field of circulation* (*Fig. 2. 2. 2*).

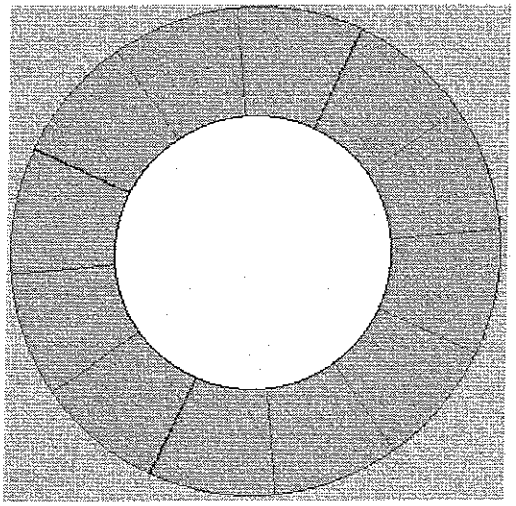

Figure 2. 2. 2. Persistent current phase structure. The lines represent a phase change cycling over 2π *for* $m = 0$.

Though superfluid persistent current is a metastable state, it can have an effectively infinite lifetime under suitable conditions. The decay of persistent current involves a change in the quantized circulation around the ring. Changes in the topology of the lines require that vortex pairs be formed and moved apart, or moved together and annihilated. At low temperatures, this might only happen under the macroscopic influences. Thinking of TASC, we may note that condensing atoms would not be able to cause such changes since they are microscopic events.

The details of a condensation event are well understood in terms of thermal excitations [2. 7]. *In principle, the impinging atom state can be expressed as a superposition of elementary excitations in the film, and it is these excitations that conserve energy and momentum for the process. The dominance of the ground state, within which the thermal excitations are considered, ensures that the condensing atom assimilates into the superfluid. The excitations eventually thermalize.*

Once created, persistent current along with its associated phase structure represents the quasi-ground state of the superfluid film with respect to which thermal excitations are referenced. This is the appropriate base state within which to consider the excitations since it is the state, described by the wavefunction $\psi_{0\ p.c.}(r,\ t)$, *the superfluid film would be left with as the temperature were reduced to zero. Therefore, the wave function* $\psi_{p.c.}$ *of persistent current at finite temperatures can be expressed as the following:*

$$\psi_{p.c.}(r,\ t) = \psi_{0\ p.c.}(r,\ t) + \sum_{K} C_K \phi_K, \qquad (2.\ 2.\ 2)$$

where the excitations are accounted for by the sum.

Now consider third sound mode in the superfluid helium film. The flow field is oscillatory in nature and also thermally active. The mode is consequently not persistent to the same extent as a DC flow. There are several aspects of this situation to keep in mind. One of them is related to the phase structure. The third sound wavelength $\lambda_3 = 2\pi / k$ *is on the order of a centimeter and its associated velocity field extends over this wavelength. The velocity field of third sound mode has its own quantum phase structure (Fig. 2. 2. 3) which, as in the case of persistent current, is also described by* $\hbar \nabla \varphi / m_4$ *as in equations (1. 4. 3) and (2. 2. 1).*

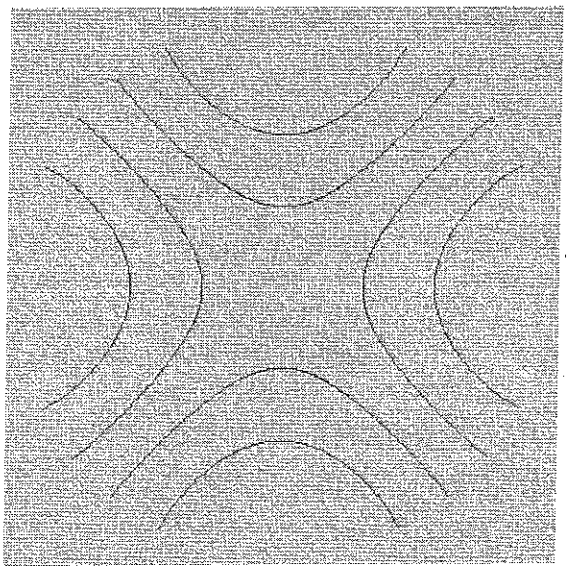

Figure 2. 2. 3. Instantaneous third sound (2, 1) mode phase structure. The lines represent a phase change cycling over 2 π for $m = 2$.

Combined with the equations of motion (2. 1. 2 − 3), the phase structure of third sound wave acquires the form as shown in equation (2. 2. 3) below, where h_o is usually around 3 nm in our experiments.

$$\varphi = \frac{c_3 m_4}{\hbar k}\left(\frac{\eta}{h_o}\right) \qquad (2.\ 2.\ 3)$$

Another aspect to consider is a microscopic amplitude regime, where third sound itself is a part of the elementary excitation spectrum (Fig. 1. 3. 2) of the superfluid helium in thermal equilibrium. Thermally populated to a harmonic oscillator level of $n = 10^6$, *given by the Plank distribution at* $T = 0.1\ K$, *third sound amplitude would cause insignificant phase oscillations that might vary only slightly over the wavelength of the third sound.*

And finally, very important for the TASC project is a macroscopic flow regime, when third sound is classically driven to quite high amplitudes. For comparison, an amplitude with $\eta / h_0 = 0.01$ *will correspond to the equivalent harmonic oscillator excitation level of* $n = 10^{18}$. *In this situation the quantum phase structure would have a wavelength on the order of 50* μm *which is still much smaller than third sound wavelength. Although the wave is quite classical, with an extremely high level of excitation, the instantaneous flow field is well describedd by a quantum phase (Fig. 2. 2. 3) structure similar to the persistent current (Fig. 2. 2. 2) case, with a flow of 20 cm / sec here.*

Thus, third sound wavefunction ψ_S *might be presented by equation (2. 2. 4)*

$$\psi_S(r,\ t) = \psi_{0S}(r,\ t) + \sum_q C_q \phi_q, \qquad (2.\ 2.\ 4)$$

reflecting the fact that thermal excitations are referenced now to the macroscopic

quantum phase structure of the third sound mode for their zero occupation base state – the mode being a well defined state, described by $\psi_{0\,S}$, *as the film temperature is reduced to zero.*

Condensing atoms therefore will be assimilated into the quantum phase structure of the classical third sound flow field, preserving the local character of the phase structure, the local character being the film velocity. Within the classical velocity field of the third sound wave, microscopic condensation events are indistinguishable from those in persistent current, both of which stimulate atoms to condense coherently into the given phase structure due to overwhelming occupation of the Bose state.

■ 2.3 Quantum condensation and third sound amplification

In the process of quantum condensation [2. 7] helium atoms from the vapor become affiliated with the velocity field of persistent current circulation state [1. 36]. As a result, the superfluid component absorbs the mass, and the excitations, making up the normal component, account for balance of the energy and momentum of the condensing atom.

If the moving film is a persistent current adsorbed onto the surface of the ring (Fig. 2. 2. 1), both the angular momentum and the energy of the superfluid are increased proportionally to the increase in the mass of the film. Of course, angular momentum and energy are conserved, with the excitations deposited in the film assuring a proper accounting of the former. The angular momentum and energy changes experienced by the condensing vapor atoms as they assimilate into the moving film will ultimately be transmitted to the substrate as the excitations thermalize.

Rewriting equation (2. 2. 1) in the form

$$m_4 r v_S(r) = n \hbar, \qquad (2.3.1)$$

we see that the angular momentum per atom is quantized in units of $\hbar$ at any position in the film. The condensation thus converts heat into mechanical energy. This energy shows up as a thicker film moving with the constant flow speed. As appears, it is not possible to remove the added atoms by the film flow in some continuous process that leaves the energy of persistent current behind as an increased circulation speed (Fig. 2. 3. 1).

When atoms are removed from the flow region, their kinetic energy is removed

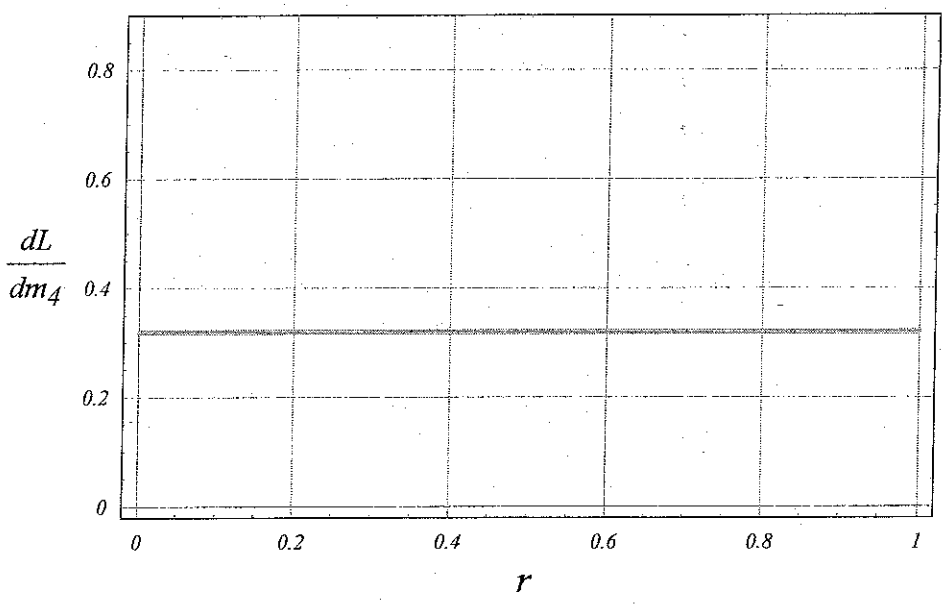

Figure 2. 3. 1. Scaled angular momentum distribution for the persistent current depicted in Fig. (2. 2. 1).

with them because any extraction path away from the flow is subject to the same potential flow constraints that give rise to the quantized circulation condition (2. 2. 1), and will preserve the velocity.

Vapor condensation can add energy and angular momentum to either persistent current flow field or third sound wave flow field. The difference in the rate of growth of the angular momentum versus energy illustrates an interesting feature of the acoustic mode case. The acoustic mode holds the energy and momentum in a distinctly different way than persistent current. First of all, only half of the energy in the acoustic

mode is kinetic, where it is all kinetic in the persistent current. Secondly, the angular momentum of a persistent current is derived from extended circulation of the super-fluid, as in equation (2. 2. 1). Acoustic angular momentum has its roots in the small oscillatory orbital motion of fluid elements within a field of zero circulation.

We saw that a persistent current would loose its energy and momentum if mass were drained away by a film flow, preserving the circulation. This is not the case for third sound acoustic mode that has its angular momentum contained (Fig. 2. 3. 2) in

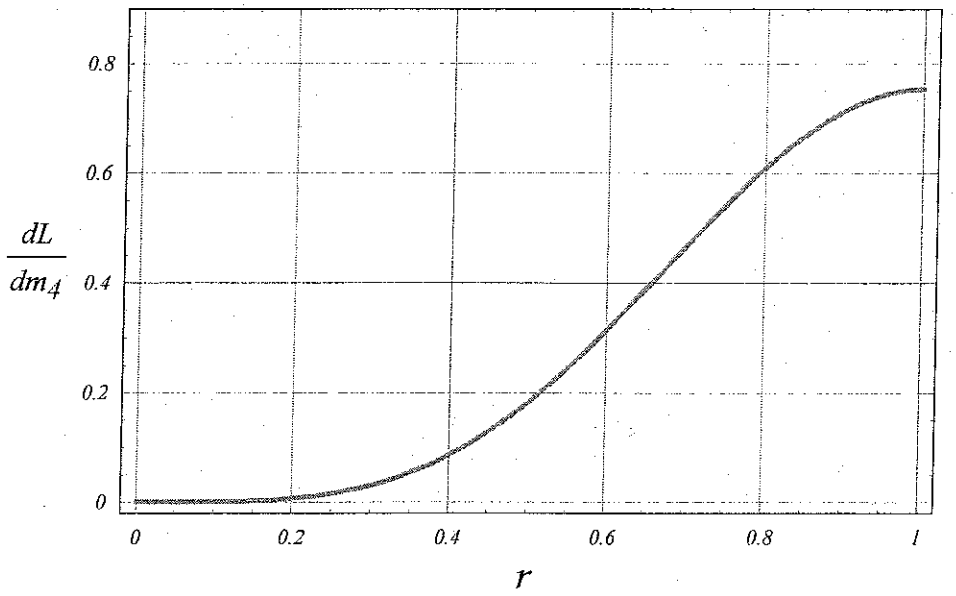

Figure 2. 3. 2. Scaled angular momentum distribution for third sound (2, 1) mode depicted in Fig. (2. 1. 2

the localized film oscillations. As film mass is removed from the resonator by an axi-symmetric, radial DC flow, the angular momentum of the oscillatory acoustic mode

will be preserved [2. 6]. *The energy of mode actually increases, receiving the work done against the substrate potential as film is pulled away, but the excitation level, being proportional to L, is constant.*

With this decoupling of the acoustic mode from the DC film flow, a continuous input of energy, through vapor condensation and simultaneous mass extraction, can be achieved.

The energy gain is proportional to the energy stored in the mode, and will have the effect of reducing the dissipation of the third sound mode. This is a continuous process of third sound gain which, when large enough, will result in a self-oscillation.

The condition for this self-oscillation can be written in terms of the free mode quality factor Q *and AC energy* $\mathcal{E}_{ac}$ *input into a chosen third sound mode described by its frequency* ω_{mn} *and energy* $\mathcal{E}_{res}$ [2. 8].

$$\frac{d\,\mathcal{E}_{ac}}{d\,t} \geq \frac{\omega_{mn}\,\mathcal{E}_{res}}{Q} \quad or \quad \frac{d\,h}{d\,t} \geq \frac{2}{5}\,\frac{\omega_{mn}\,h_o}{\alpha\,Q} \qquad (2.3.2)$$

This indicates the condition for a self-oscillation which requires that approximately all of the atoms in the film be replaced within the natural free decay time of the resonance for a given third sound mode. Thus, a continuous process of third sound amplification by stimulated condensation (TASC) should accompany a condensing helium vapor flux under the right conditions.

■ 2.4 Resonator design

To detect third sound amplification by stimulated condensation (TASC), the input power must be noticebale relative to the other dissipative mechanisms associated with the third sound. This thesis presents a novel resonator configuration [2. 9] that satisfies all of the following requirements : the resonator must be open to the vapor source to expose the flow antinodes of third sound wave to the vapor flux of ^{4}He atoms; it must be mechanically supported and coupled to transducers in a way that minimizes third sound radiation; it also must be able to dissipate both the latent heat and the mass of the condensing helium atoms; and, finally, the third sound must have an inherently high quality factor.

The resonator cross section is shown in Fig. 2. 4. 1 below. It consists of a vapor source (a) having a loop − shaped form and independently supported above a flat sapphire disk (b). The disk is coated on all its surfaces with evaporated silver and epoxied to a central post in a copper base (d). Four other posts in the base support a square circuit board plate (c) the upper surfaces of which are patterned into four polished copper capacitive transducers.

The superfluid helium film coats the upper and lower sides of the disk as well as all other surfaces in the experimental chamber enclosing the apparatus. The top surface of the disk is open to the flux of vapor atoms which can be varied by changing the power of heater loop. The film on the bottom surface of the disk is within the capacitor gaps for both driving and detecting.

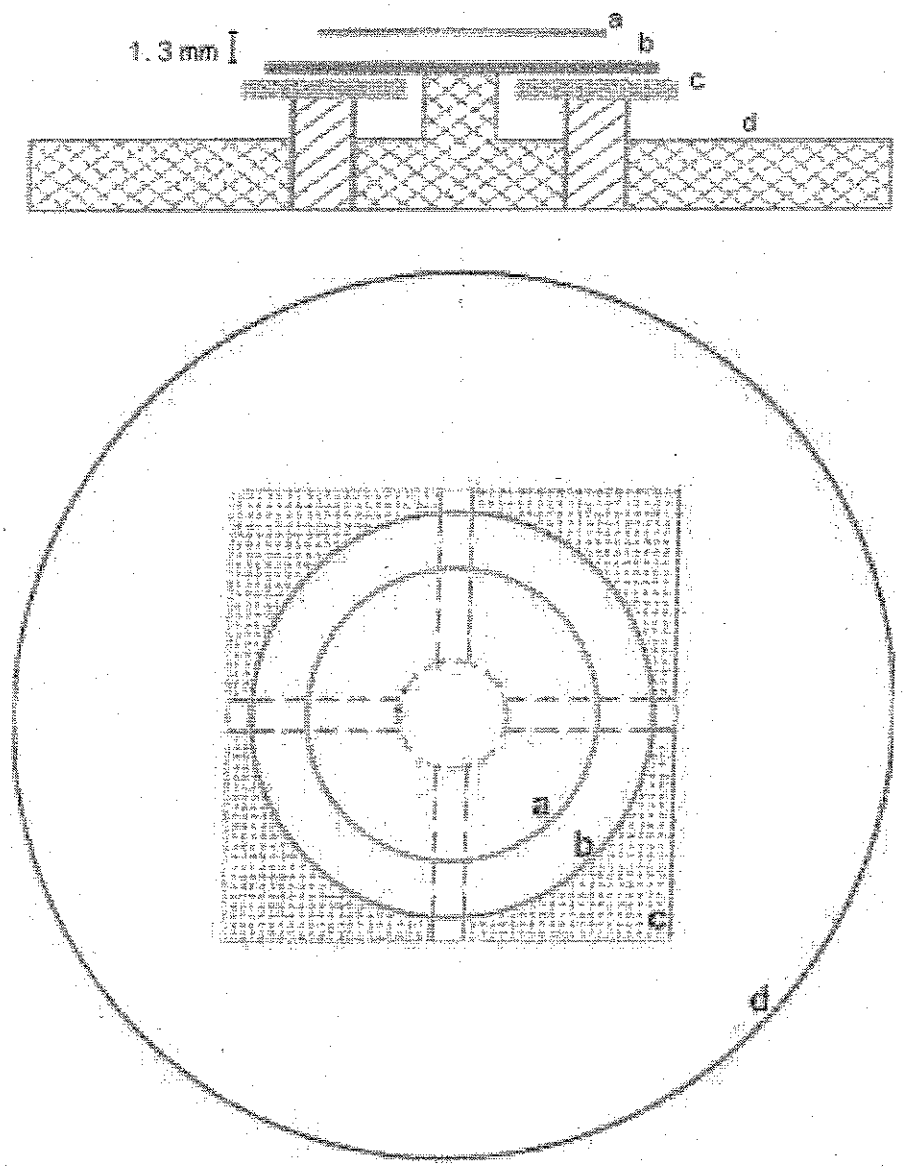

Figure 2. 4. 1. Schematic of the third sound resonator : a – heater, b – sapphire disk, c – capacitor plates, d – base with a central post.

All numerical values below are the product of our thorough theoretical modeling and calculations in Chapter 3 and will be used here to give a better understanding

of the requirements imposed on the resonator in order to observe the TASC.

Thus, to maximize the sensitivity to the input power, the third sound resonator design was based on a target Q of 10^5 associated with each of the several dissipation mechanisms. Thermo – mechanical dissipation through vapor coupling in the open geometry, for example, requires working temperatures stay below 0.26 K, where the equilibrium vapor pressure rapidly diminishes. Consideration of the radiation down the central post from a specified 13 mm diameter disk imposes constraints on both the length and diameter of the post. The mechanical stability of the resonator excluded working with the lowest $m = 1$ mode but a 3 mm long by 2.4 mm diameter central post proved to be sufficient for the lowest $m = 2$ third sound mode. The transducers are optimized for a coupling to this mode with the added advantage of insensitivity to any lateral vibrational swaying of the disk.

Finally, consideration of the vapor flux distribution requires some care in the design of the source ring. We wish to deposit the maximum amount of vapor over the flow antinodes of the $m = 2$ mode with constraints on the maximum flux impiging the film (causing local heating of the film), the total latent heat that must be dissipated by the resonator into the base, and the overall total heater power required by the ring. A heater with a ring diameter of 9 mm placed 1.3 mm above the resonator disk was a reasonable compromise.

Previous experience with closed resonators [2. 10] suggested working with moderately thick helium films of 8 – 12 layers which was in a good agreement with our theoretical estimates. We also expect that a deposited power of 1 μ W might challenge the conductance of the whole system, causing the maximum temperature in the film to rise

above our working limit of 0.26 K. At values below this one, we anticipate that the input power will be easily distinguished by a decrease in the overall $(Q^{-1})_{TASC}$ *energy losses proportional to the applied vapor source heater power.*

A working prototype of the described third sound resonator has been already assembled (Chapter 4) and our first experimental data obtained with it are discussed (Chapter 5) below.

Chapter 3. Theoretical Modeling

Detailed calculations on the optimal resonator geometry to detect third sound amplification due to stimulated condensation of helium vapor atoms into a resonating (2, 1) mode are presented in this chapter. The ultimate question on how TASC effect can be observed is answered as well.

3.1 Flux formula

The amount of flux of helium atoms entering the film from the vapor is an important factor to know in our calculations in a proper resonator design.

Consider, therefore, a ring of radius $\mathcal{R}$, centered a distance z above the resonator disk of radius a (Fig. 3. 1. 1). We need to obtain the expression for the flux $\mathcal{F}$ of atoms on the disk at some point P situated a distance r from the origin O and a distance s from the ring element $d\ell$ which is assumed to operate as a point source with a uniform flux density $\lambda_{\mathcal{F}} = d\mathcal{F} / d\ell$. Recalling a standard flux definition as a number $\mathcal{N}$ of atoms impinging perpendicularly on the surface element per unit time, we arrive at the formula

Null

$$d\mathcal{F} = \mathcal{F}_o \frac{d\phi}{2\pi} = \frac{\dot{\mathcal{N}}}{4\pi s^2} \frac{z}{s} \frac{d\phi}{2\pi}, \qquad (3.1.1)$$

where $\dot{N}$ is a total number of helium atoms leaving per unit time the ring and s – is the shortest distance from the point P on the disk to that element of the ring.

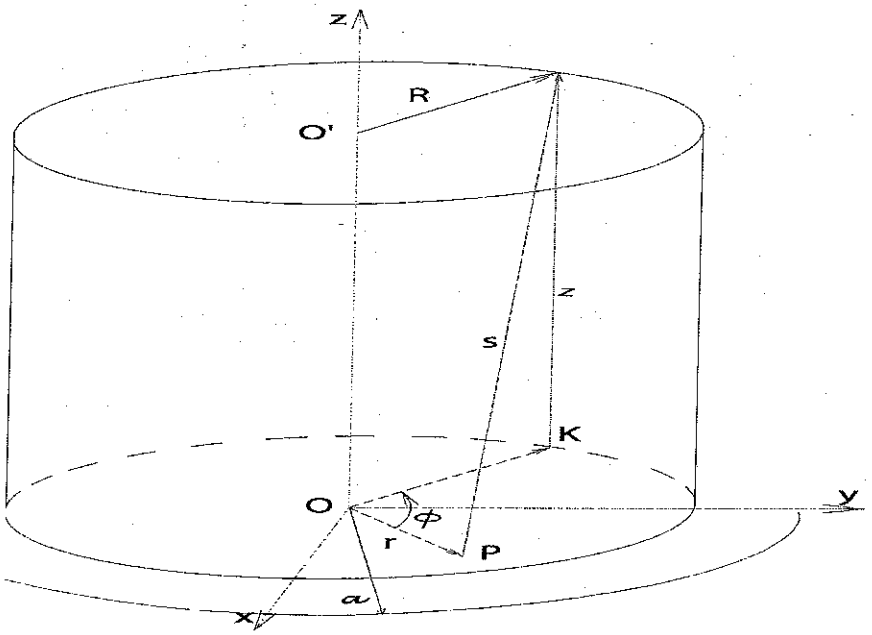

Figure 3. 1. 1. Schematic of the vapor source of radius $\mathcal{R}$ for the calculation of the flux distribution at point P.

From geometry in Fig. 3. 1. 1 we find that

$$s^2 = z^2 + \left(\vec{\mathcal{R}} - \vec{r}\right)^2 = z^2 + \mathcal{R}^2 + r^2 - 2\,\mathcal{R}\,r\cos\phi \qquad (3.\,1.\,2)$$

Since it is convinient to use dimensionless variables, we will scale all distances with respect to the radius a of our sapphire disk to have

$$\chi = r/a, \qquad \rho = \mathcal{R}/a, \qquad \zeta = z/a \tag{3. 1. 3}$$

This allows us to write down the expression for the flux at point P on the disk

$$\mathcal{F}(\chi,\ \zeta,\ \rho) = \frac{\dot{\mathcal{N}}}{8\pi^2 a^2}\ \frac{\zeta}{(\chi^2+\zeta^2+\rho^2)^{3/2}}\ \int_0^{2\pi} \frac{d\phi}{\left(1-\frac{2\chi\rho\cos\phi}{\chi^2+\zeta^2+\rho^2}\right)^{3/2}} \tag{3. 1. 4}$$

Formula (3. 1. 4) can be nicely simplified further by introducing an argument $u = 2\chi\rho/\left(\chi^2+\zeta^2+\rho^2\right)$ *under the integral which now can be written in terms of the hypergeometric [3. 1] function* ${}_2F_1\left(5/4,\ 3/4;\ 1;\ u^2\right)$.

$$\int_0^{2\pi} \frac{d\phi}{(1-u\cos\phi)^{3/2}} = 2\pi\ {}_2F_1\left(5/4,\ 3/4;\ 1;\ u^2\right) \tag{3. 1. 5}$$

Thus, the flux of helium vapor atoms striking the resonator disk at some point P a distance χ *from its center can be presented by the following expression*

$$\mathcal{F}(\chi,\ \zeta,\ \rho) = \frac{\dot{\mathcal{N}}}{a^2}\ \Phi(\chi,\ \zeta,\ \rho), \tag{3. 1. 6}$$

where

$$\Phi(\chi,\ \zeta,\ \rho) = \frac{\zeta}{8\pi^2}\ \frac{2\pi\ {}_2F_1\left[5/4,\ 3/4;\ 1;\ u^2\right]}{(\chi^2+\zeta^2+\rho^2)^{3/2}} \tag{3. 1. 7}$$

▪ 3. 2 Resonator boundary value problem

We have already learned from the previous chapter that the wave equation (2. 1. 4) describing the motion of helium film becomes the Bessel equation [2. 4] in cylindrical coordinates. Looking at our resonator geometry (Fig. 3. 2. 1), one might notice that a different wavefunction form of the film oscillations will correspond to each segment of the resonator surface. Thus, $A J_m(k r)$ *will reflect the wave motion on the top of the disk;* $A_1 J_m(k r) + B_1 Y_m(k r)$ *– on its bottom;* $A_2 e^{k_z z} + B_2 e^{-k_z z}$ *along the central post; and* $A_3 J_m(k r) + B_3 Y_m(k r)$ *– at the base.*

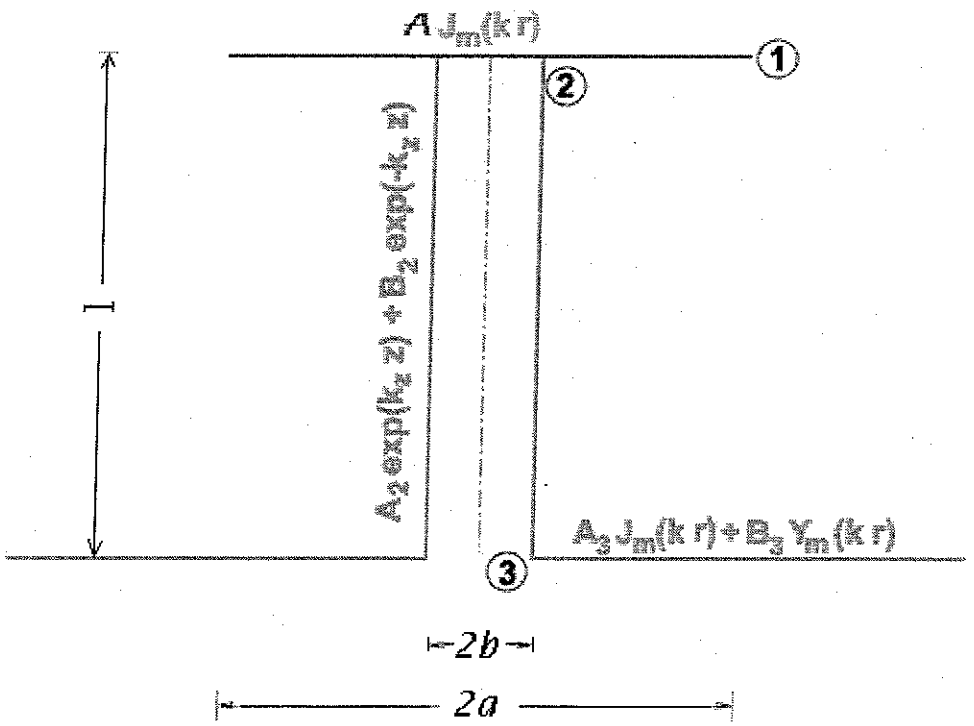

Figure 3. 2. 1. Boundary value problem for the resonator.

Since wavefunction of the film oscillations is continuous everywhere, it needs

to satisfy the boundary conditions at points 1, 2 and 3 specified by the corresponding values of r and z (Fig. 3. 2. 1). The same is also true for the wavefunction derivatives with respect to r which represent the radial film velocities at these points.

Therefore, for each of the three boundaries, we recieve three pairs of the continuity equations for the wavefunction and its derivative, correspondingly.

Thus, at $r = a$ *and* $z = 0$, *we get*

$$A\,J_m(k\,a) = A_1\,J_m(k\,a) + B_1\,Y_m(k\,a) \qquad (3.\,2.\,1\,a)$$

$$A\,J'_m(k\,a) = -A_1\,J'_m(k\,a) - B_1\,Y'_m(k\,a) \qquad (3.\,2.\,1\,b)$$

At $r = b$ *and* $z = 0$,

$$A_1\,J_m(k\,b) + B_1\,Y_m(k\,b) = A_2 + B_2 \qquad (3.\,2.\,2\,a)$$

$$A_1\,J'_m(k\,b) + B_1\,Y'_m(k\,b) = -k_z\,(A_2 - B_2)/k \qquad (3.\,2.\,2\,b)$$

At $r = b$ *and* $z = \ell$,

$$A_3\,J_m(k\,b) + B_3\,Y_m(k\,b) = A_2\,e^{k_z\,\ell} + B_2\,e^{-k_z\,\ell} \qquad (3.\,2.\,3\,a)$$

$$A_3\,J'_m(k\,b) + B_3\,Y'_m(k\,b) = k_z\left(A_2\,e^{k_z\,\ell} - B_2\,e^{-k_z\,\ell}\right)/k \qquad (3.\,2.\,3\,b)$$

As before, it is helpful to scale resonator dimensions by the radius a of the disk. For this reason, we introduce new dimensionless resonator parameters such as

$$x = k\,a, \qquad \varepsilon = b/a, \qquad \lambda = \ell/a \tag{3. 2. 4 a}$$

$$k_z/k = \sqrt{\left(\frac{m}{x\varepsilon}\right)^2 - 1}\,, \quad k_z\,\ell = x\,\lambda\sqrt{\left(\frac{m}{x\varepsilon}\right)^2 - 1} \tag{3. 2. 4 b}$$

and greatly simplify working with the equations (3. 2. 1 − 3) by conviniently presenting them in matrix forms. Thus, we can solve (3. 2. 1) to express the wave amplitude on the bottom of the disk in terms of the one on its top

$$\begin{pmatrix} A_1 \\ B_1 \end{pmatrix} = S_1{}^{-1}\,\mathcal{V}\,A, \tag{3. 2. 5}$$

where

$$S_1 = \begin{pmatrix} J_m(x) & Y_m(x) \\ J'_m(x) & Y'_m(x) \end{pmatrix} \qquad \text{and} \qquad \mathcal{V} = \begin{pmatrix} J_m(x) \\ -J'_m(x) \end{pmatrix} \tag{3. 2. 6}$$

Similarly, we derive the wave amplitude in (3. 2. 2) on the post in terms of that on the bottom of the disk

$$\begin{pmatrix} A_2 \\ B_2 \end{pmatrix} = S_{02}{}^{-1}\,S_2 \begin{pmatrix} A_1 \\ B_1 \end{pmatrix}, \tag{3. 2. 7}$$

where

$$S_{02} = \begin{pmatrix} \frac{1}{-\sqrt{\left(\frac{m}{x\varepsilon}\right)^2 - 1}} & \frac{1}{\sqrt{\left(\frac{m}{x\varepsilon}\right)^2 - 1}} \end{pmatrix} \text{ and } S_2 = \begin{pmatrix} J_m(x\varepsilon) & Y_m(x\epsilon) \\ J'_m(x\varepsilon) & Y'_m(x\varepsilon) \end{pmatrix} \quad (3.2.8)$$

And, finally, from (3. 2. 3), we get the expression for the wave amplitude at the base

$$\begin{pmatrix} A_3 \\ B_3 \end{pmatrix} = S_2^{-1} S_{03} \begin{pmatrix} A_2 \\ B_2 \end{pmatrix}, \quad (3.2.9)$$

where

$$S_{03} = \begin{pmatrix} e^{x\lambda\sqrt{\left(\frac{m}{x\varepsilon}\right)^2 - 1}} & e^{-x\lambda\sqrt{\left(\frac{m}{x\varepsilon}\right)^2 - 1}} \\ \sqrt{\left(\frac{m}{x\varepsilon}\right)^2 - 1}\, e^{x\lambda\sqrt{\left(\frac{m}{x\varepsilon}\right)^2 - 1}} & -\sqrt{\left(\frac{m}{x\varepsilon}\right)^2 - 1}\, e^{-x\lambda\sqrt{\left(\frac{m}{x\varepsilon}\right)^2 - 1}} \end{pmatrix} (3.2.10)$$

It means, that for given resonator parameters such as x, ℓ and λ we can answer the question on how the third sound wave will eventually propagate out of the resonator by knowing its wave amplitude at the bottom

$$\begin{pmatrix} A_3 \\ B_3 \end{pmatrix} = S_2^{-1} S_{03} S_{02}^{-1} S_2 S_1^{-1} \mathcal{V} A \quad (3.2.11)$$

It appears to be very useful information in designing the resonator with a high Q.

▪ 3.3 Resonator's Q due to its geometry.

The quality factor Q by definition [3. 2] is determined as

$$Q = 2\pi \frac{\text{average energy stored per period}}{\text{energy loss per period}} \qquad (3.3.1)$$

In the case of free third sound (m, n) mode of frequency ω_{mn}, (3. 3. 1) transforms to

$$Q_g = \frac{\omega_{mn}\, \mathcal{E}_{res}}{\dot{\mathcal{E}}_{ac}}, \qquad (3.3.2)$$

where $\mathcal{E}_{res}$ is the energy of the mode averaged over the period $\mathcal{T}$ and $\dot{\mathcal{E}}_{ac}$ is the average power dissipated over that period.

From the equation of motion (2. 1. 3) for the superfluid film of quiescent thickness h_0, we find a relation between its velocity v and a waveform η of film oscillations.

$$v(r) = c_3 \frac{\eta(r)}{h_0} \qquad (3.3.3)$$

We incorporate this result in the expression for the total energy density, energy per area, of the third sound wave (with superfluid helium density ρ)

$$\mathcal{U} = \frac{1}{2} v^2 \rho h_o = \frac{1}{2} c_3{}^2 \left(\frac{\eta}{h_o}\right)^2 \rho h_o, \qquad (3.3.4)$$

which then is integrated over the whole area $\mathcal{A}$ of our resonator disk with radius a and averaged over $\mathcal{T}$ to find the energy of a resonating third sound mode.

$$\mathcal{E}_{res} = \prec \int \mathcal{U}\, d\mathcal{A} \succ_{\mathcal{T}} = \frac{\pi a^2}{x_m{}^2} c_3{}^2 \left(\frac{A}{h_o}\right)^2 \rho h_o J^2{}_{rms}, \qquad (3.3.5)$$

where A is the amplitude of film oscillations on the disk, values x_m are solutions of the equation $J_m{}'(x_m) = 0$, and $J^2{}_{rms}$ is calculated below

$$J^2{}_{rms} \equiv \int_0^{x_m} u\, J_m{}^2(u)\, du = \frac{1}{2}\left(x_m{}^2 - m^2\right) J_m{}^2(x_m) \qquad (3.3.6)$$

Far away, the radial solution $\eta(r) = A_3 J_m(k r) + B_3 Y_m(k r)$ at the base will exhibit an asymptotic sinusoidal variation with $kr >> 1$ and can be approximated

$$\eta(r) \simeq \sqrt{\frac{2}{\pi k r}} \left[A_3 \sin\left(kr - \frac{m\pi}{2} - \frac{\pi}{4}\right) + B_3 \cos\left(kr - \frac{m\pi}{2} - \frac{\pi}{4}\right)\right] \qquad (3.3.7)$$

In the limit of $r \to \mathcal{R}$, the wave will travel over the area of $2\pi \mathcal{R} c_3 \Delta t$, and for the energy dissipation we get

$$\dot{\mathcal{E}}_{ac} = \frac{1}{2} c_3^2 \frac{A_3^2 + B_3^2}{h_o^2} \rho h_o \frac{c_3}{k} \qquad (3.3.8)$$

Substituting the results of equations (3. 3. 5) and (3. 3. 8) as well as (2. 1. 6) in formula (3. 3. 2) will provide us with the expression for the resonator's quality factor Q_g due to its geometry, equation (3. 3. 9), and optimal resonator parameters, Fig .3. 3. 1.

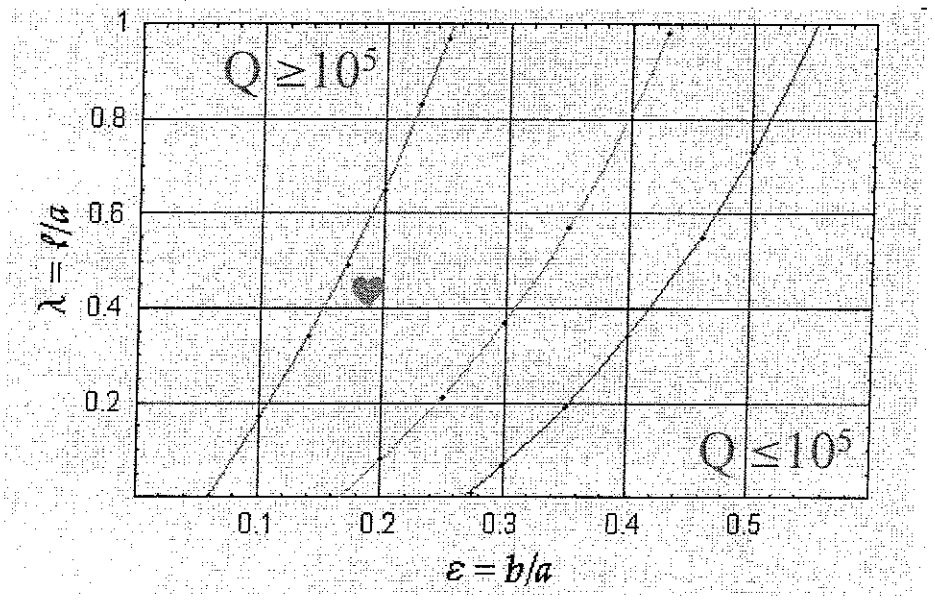

Figure 3. 3. 1. Optimal resonator geometry for three third sound modes. Black dots – calculations – represent scaled values of ℓ and b to satisfy the requirement of $Q \geq 10^5$. Lines red, green and blue are the interpolation of these values or (1, 1), (2, 1) and (3, 1) modes, correspondingly.

$$Q_g = \pi \left(x_m^2 - m^2 \right) J_m^2 (x_m) \frac{A^2}{A_3^2 + B_3^2} \qquad (3.3.9)$$

Since we have already (3. 2. 11) calculated the oscillation amplitudes A_3 and B_3 in terms of A, equation (3. 3. 9) proves to be a guidance for us in the process of resonator design.

$$Q_g = \frac{\pi \left(x_m^2 - m^2 \right) J_m^2 (x_m)}{|S_2^{-1} S_{03} S_{02}^{-1} S_2 S_1^{-1} \mathcal{V}|^2} \qquad (3.3.10)$$

Equation (3. 3. 10) suggests the optimal resonator dimensions such as length ℓ of the central post and its radius b for the given disk of radius a and a fixed $Q \geq 10^5$.

Scaled geometry of the resonator with a quality factor $Q \geq 10^5$ for the three third sound (1, 1), (2, 1) and (3, 1) modes is shown in Fig. 3. 3. 1 above. The actual resonator dimensions such as length of its central post, $\ell = 3$ mm and its radius, $b = 1.2$ mm for the (2, 1) third sound mode are depicted by the heart sign.

▪ 3. 4 Third sound Q due to vapor coupling

Due to the fact that our resonator is open to the helium vapor, there are some consequences which affect the values of Q. Therefore, some aspects of the proposed resonator design certainly need to be addressed. Radiation of the third sound along the supporting post has been studied in the previous section; and losses related to the thermal contact with a vapor surrounding the disk will be considered here.

In the equilibrium, saturated vapor pressure could be determined from the Clausius – Clapeyron equation [3. 3] as

$$P_S = P_O \, e^{-T_O/T}, \qquad (3.4.1)$$

where P_O and T_O are the reference points on the vapor – liquid coexistence curve. And for helium they are known to have the values : $T_O = 7.16\ K$ and $P_O = 10^5\ Pa$.

Unsaturated film pressure P_f, in turn, depends on a strength of the Van der Waals attractive potential [3. 4] described by T_v, and is the following,

$$P_f = P_S \, e^{-T_v/\left(T\, d^3\right)} \qquad (3.4.2)$$

Film thickness h_O enters formula (3. 4. 2) as a number d of film layers and is scaled by a thickness $h_1 = 3.6\ Å$ of one layer of helium atoms.

Open resonator geometry allows a maximum exposure to the vapor flux $\mathcal{F}$ of helium atoms which can be studied either in terms of an equilibrium film pressure P_f or effective heat transfer $\dot{q}$ to the film.

Latter approach, which we have decided to choose, will introduce an effective thermal heat sink with

$$\dot{q} = \sigma \mathcal{A} \Delta T, \tag{3. 4. 3}$$

characterized by a thermal conductance σ, to describe a coupling to the vapor flux

$$\mathcal{F}(T) = \frac{P_f}{\sqrt{2 m_4 \kappa_b T}} \tag{3. 4. 4}$$

which can be employed to described a heat transfer to the film in the following manner

$$\dot{q} = \mathcal{L} \Delta \mathcal{F} \mathcal{A} \tag{3. 4. 5}$$

Combining equations (3. 4. 3 – 5), we find the expression for a thermal conductivity in the form of the flux partial derivative with respect to the temperature T, multiplied by two constants : Boltzman's, κ_b and helium atom latent heat, $\mathcal{L} = 7.16\ K$.

$$\sigma(T, d) = \kappa_b \mathcal{L} \partial_T \mathcal{F}(T, d) \tag{3. 4. 6}$$

Sensitive to the environment third sound will experience a relaxation rate γ_T

$$\gamma_T(T,\ d) = \frac{\dot{q}}{q} = \frac{\sigma(T,\ d)}{\rho\, h_0(d)\, C(T,\ d)} \qquad (3.\ 4.\ 7)$$

caused by a surrounding helium vapor that reduces values of quality factor Q_0 *of the third sound resonance. Presented above formula (3. 4. 7) includes helium density* $\rho = 145\ kg/m^3$, *helium film thickness* $h_0(d)$ *in number* d *of layers, and helium specific heat* $C(T,\ d)$ *as a function of temperature and film thickness.*

Therefore, one might analyse the situation above in terms of the third sound losses Q_{vap}^{-1} *by employing values* Q_0^{-1} *that reflect a ratio of mechanical energy to thermal energy in the film :*

$$Q_{vap}^{-1} = Q_0^{-1}\left(\frac{\omega_{mn}}{\gamma_T} + \frac{\gamma_T}{\omega_{mn}}\right)^{-1} \qquad (3.\ 4.\ 8)$$

which include vapor damping γ_T *and depend on resonating mode. Angular frequency of third sound* $(m,\ n)$ *mode is given by* ω_{mn} *and is eventually determined by a thickness of helium film (2. 1. 6).*

All available information on helium films was used to collect data on specific heat $C(T,\ d)$ *and* $Q_0^{-1}(T,\ d)$ *as functions of temperature for a particular film thickness (see Appendix 1). Then these data were fitted to produce analytical ex-*

pressions for $C(T, d)$ and $Q_o^{-1}(T, d)$ which finally allowed us to utilize them in formulae (3. 4. 7) and (3. 4. 8).

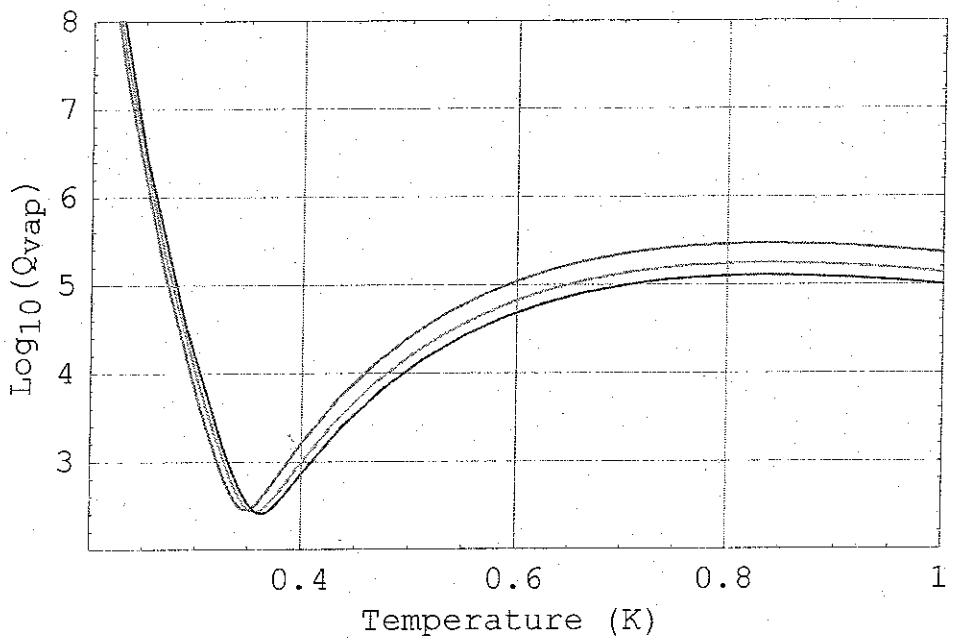

Figure 3. 4. 1. Explicit temperature dependencies of Q_{vap} for three third sound modes having film thickness of ten layers. Lines red, green and blue represent (1, 1), (2, 1) and (3, 1) modes, correspondingly.

Expecting our third sound quality factor Q_d to be at least around 10^5, we wanted to know how strongly it might be affected by the presence of helium vapor. Figure 3. 4. 1 above shows for this reason the Q_{vap} temperature dependencies for three third sound modes. It is clear from Figure 3. 4. 1 that in order to have Q of third sound within 10^5, we definitely need to work with these modes below $T \approx 0.26\ K$.

It is also important to know what is the optimal thickness of helium film might be to satisfy the requirement of $Q \approx 10^5$ in the vapor environment. The answer to this question is given by Figure 3. 4. 2 below where maximum allowed working temperatures for particular third sound modes and helium film thicknesses are shown below.

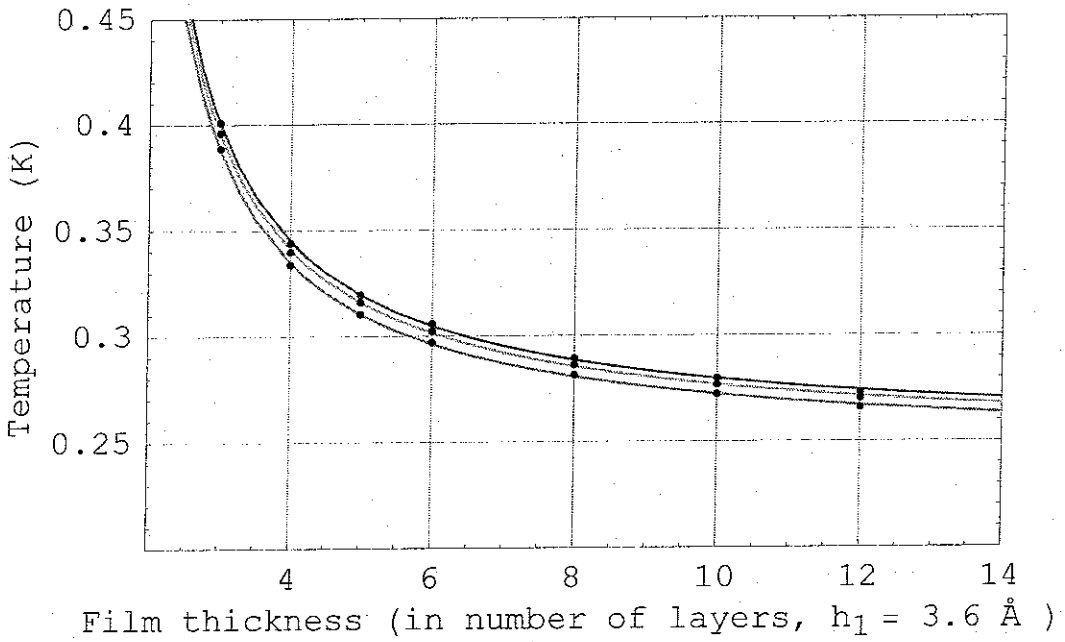

Figure 3. 4. 2. Maximum allowed working temperatures for three third sound modes with $Q_{vap} \geq 10^5$. Lines red, green and blue represent (1, 1), (2, 1) and (3, 1) modes, correspondingly. Dots represent calculated values, lines – their fit.

Thus, we conclude that in the presence of vapor and reasonable film thickness of ten – fourteen layers, the most efficient working regime to observe the third sound with $Q \simeq 10^5$ will be at temperatures below $T \approx 0.26\ K$.

■ 3.5 Optimal heater parameters

We need to build and position our heater in such a way to satisfy some requirements on the amount of AC power input $\mathcal{P}_{ac}$ added to the third sound wave, critical DC power $\mathcal{P}_{dc}$ deposited on the resonator disk in the form of heat and critical values of $\mathcal{Q}$, necessary to sustain third sound oscillations.

We define $\mathcal{P}_{ac}$ and $\mathcal{P}_{dc}$ in the following way as :

$$\mathcal{P}_{ac} = \int_{disk} \mathcal{F} < \frac{m_4 v^2}{2} >_{\mathcal{T}} d\mathcal{A} \qquad (3.5.1)$$

$$\mathcal{P}_{dc} = \int_{disk} \mathcal{F} \mathcal{L} k_b d\mathcal{A} \qquad (3.5.2)$$

where the integration is performed over resonator's disk area $\mathcal{A}$ and flux $\mathcal{F}$ of vapor atoms is multiplied above by the averaged over the period $\mathcal{T}$ kinetic energy of third sound quanta and latent heat $\mathcal{L}$ of helium atom, correspondingly.

Detailed calculations of the integrals above are performed in the Appendix 2. Here we present the final results. Thus,

$$\mathcal{P}_{ac} = \frac{\dot{\mathcal{N}}}{4} \pi m_4 {c_3}^2 \left(\frac{\eta_o}{h_o}\right)^2 L_{mn}(\zeta, \rho), \qquad (3.5.3)$$

where $L_{mn}(\zeta, \rho)$ *is a numerical coefficient that depends on a third sound mode* (m, n) *under consideration and is determined by the values of the corresponding numerical integration (see Appendix 2) and scaled heater parameters,* ζ *and* ρ. *Number of vapor atoms per unit time* $\dot{\mathcal{N}}$ *leaving the ring in formula (3. 5. 3) can be controlled by the magnitude of DC power,*

$$\mathcal{P}_{dc} = 2\pi f(\zeta, \rho)\, \mathcal{W} \qquad (3.5.4)$$

deposited on the resonator disk as a part of the total heat $\mathcal{W}$ *applied to the ring*

$$\mathcal{W} = \dot{\mathcal{N}}\, \mathcal{L}\, k_b \qquad (3.5.5)$$

Coefficient $f(\zeta, \rho)$ *in formula (2.5.4) is a result of numerical integration (see Appendix 2) and depends on our heater parameters,* ζ *and* ρ, *as well.*

Since, by the assumption, AC energy $\mathcal{E}_{ac}$ *contributes constructively to the third sound, we want to maximize the former without film overheating. Therefore, by making use of formulae (3. 5. 3 – 5) for a given heater power* $\mathcal{W}$, *we can find the optimal way of increasing AC power input* $\mathcal{P}_{ac}$ *into third sound mode of our interest. Another words, we get the optimal parameters* (ζ, ρ) *of the heater ring (Fig. 3. 5. 1) in terms of its radius and height above the resonator disk to satisfy the requirement of maximum vapor flux* $\mathcal{F}$ *(3. 1. 6) and, consequently, AC power input, formula (3. 5. 1), into (2, 1) mode defined by its angular frequency* ω_{21}.

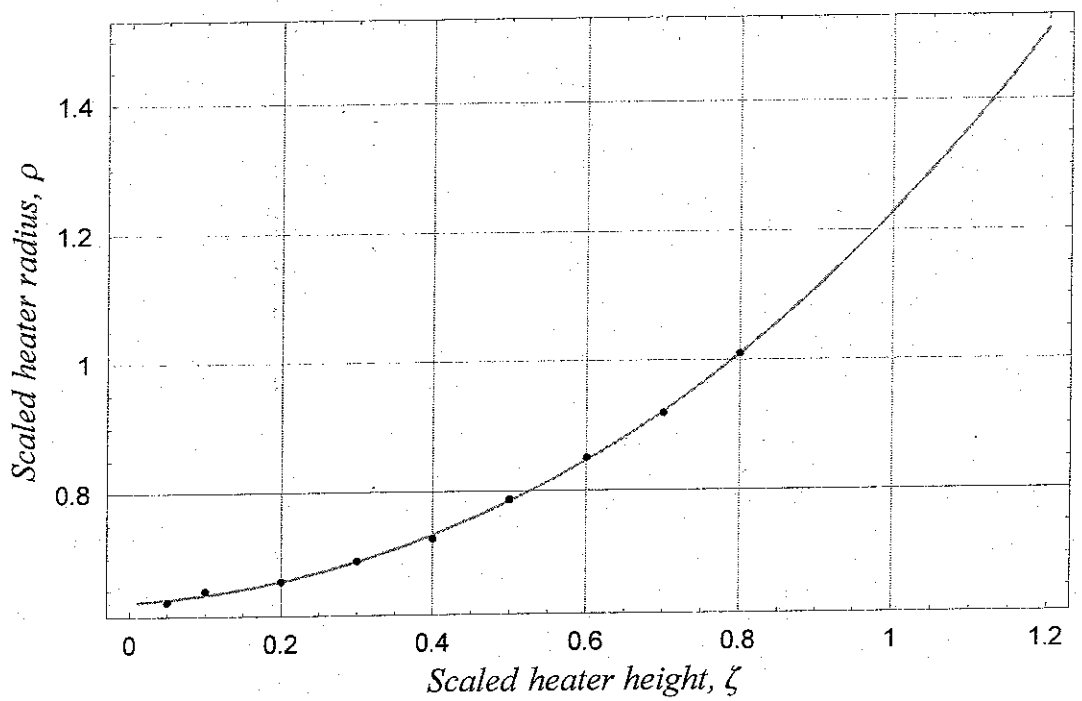

Figure 3. 5. 1. Optimal parameters for the vapor heater with both scaled radius $\rho = \mathcal{R} / a$ *and position* $\zeta = z / a$ *above the resonator disk of radius* $a = 6.5$ *mm Dots represent calculations of* (ζ, ρ) *pairs, and line is their fit.*

As it appeared, not every pair of (ζ, ρ) *numbers in the figure above will be acceptable for the actual heater parameters. To finally select a right one, we need to consider a critical situation when a balance between the energy input into third sound mode and dissipation of the latter, defined by a critical quality factor* Q_C, *has been reached eventually. Mathematically it can be expressed as the following :*

$$Q_C = \omega_{mn} \frac{\mathcal{E}_{res}}{\mathcal{P}_{ac}}, \qquad (3.5.6)$$

where the energy $\mathcal{E}_{res}$ of third sound mode has already been introduced before in formulae (3. 3. 2) and (3. 3. 5) above. Thus, for a given third sound speed c_3 and heater power $\mathcal{W}$, our best choice will be (0.2, 0.66) pair as an agreement between optimization procedure and the experimental implementation of its result.

Therefore, for (2, 1) third sound mode, we can explicitly elaborate the conditions (2. 3. 2) and express the magnitude of the critical quality factor (Appendix 2)

$$Q_c(c_3, \mathcal{W}) = \frac{0.0307}{\mathcal{W}} \sqrt[3]{c_3^4} \qquad (3.5.7)$$

to be one of the working conditions of the third sound self-oscillation when the heater power is turned on. Note that higher values of heater power $\mathcal{W}$ will reduce the critical magnitude of Q required for self-oscillation to occur.

▪ 3.6 TASC observation

By turning on the heater, we might significantly challenge a conductance of the whole system, causing the maximum temperature in the film to rise above our working limit of 0.26 K. Since we operate in millikelvin regime, a thermal boundary resistance, known as the Kapitza resistance $\mathcal{R}_K$ is considered to be mainly responsible for it.

When a heat flux $\dot{J}_q$ passes through the boundary between two materials, a temperature difference

$$\Delta T = \dot{J}_q \mathcal{R}_K \qquad (3.6.1)$$

will appear across it [3. 5]. Electrons and phonons are heat carriers in metals whereas only phonons transport heat in the insulators. Electron scattering by impurities is a dominant term in metal thermal resistance that determines $\mathcal{R}_K \propto T^{-1}$ dependence at low temperatures and usually might be reduced by a good electronic contact.

In the absence of any electronic conduction, the boundary resistance between two different dielectric substances or a dielectric and metal in contact has $\mathcal{R}_K \propto T^{-3}$ dependence and can be explained by means of the acoustic mismatch theory [3. 6].

Kapitza thermal resistance will also exist between liquid helium and a solid boundary immersed in the helium bath. Another important manifestation of Kapitza thermal resistance is an appearence of temperature difference across two solids bound

by a glue below 1 K.

These two examples are of practical interest for us since our third sound resonator is immersed in the helium bath and includes some components joined by epoxy as well (see Chapter 4).

Extracted from the experimental data [3. 7] and related to our resonator design, temperature dependencies for the Kapitza thermal resistances were utilized in our calculations to estimate a temperature rise in helium film having been taken at particular initial temperatures when a heater power was turned on (Fig. 3. 6.1).

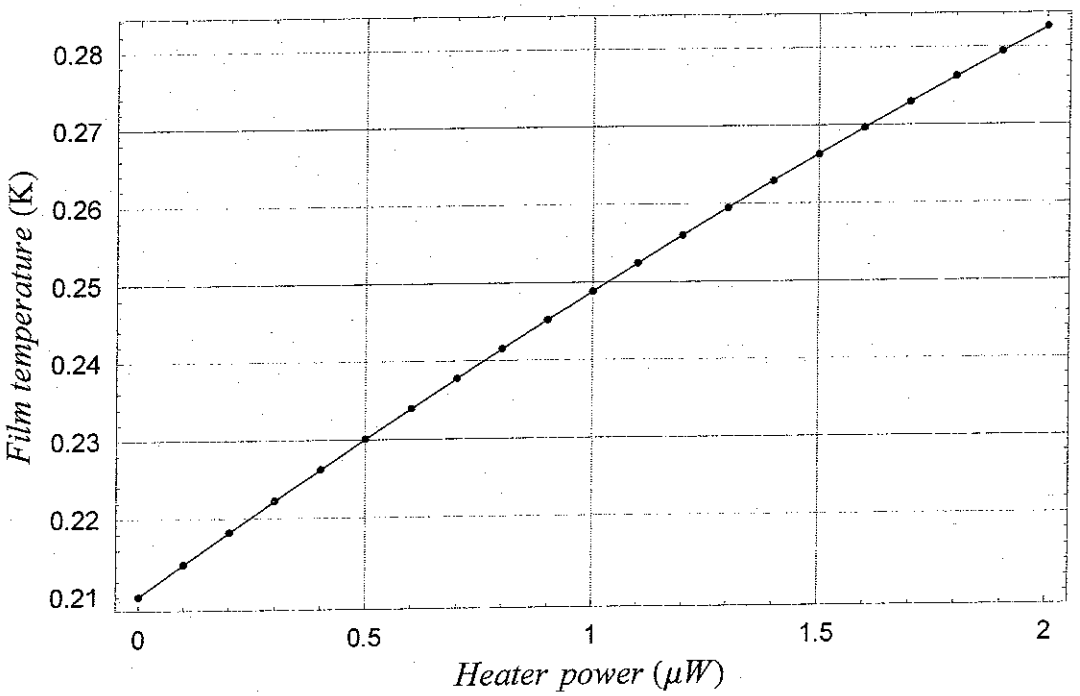

Figure 3. 6. 1. Helium film temperature rise after heater power was turned on. Dots are calculated values and line is their fit for the initial film temperature of 0.21 K.

The least response to the heater power was found in our calculations to correspond to helium film initial temperature of 0.21 K and is shown above (Fig. 3. 6. 1). As we may notice, the heater power of 1.5 μW is extensive enough to challenge our maximum allowed working temperatures of 0.26 K (see Chapter 3. 4).

Once helium film temperature response to the applied heater power is known, we might be able to answer the ultimate question of how we are going to observe our TASC. Recall that all feasible losses pertaining to the experiment have been already accounted for in the previous chapters since they could be simply expressed as the inverse of the corresponding quality factors. Therefore, the overall TASC losses, $(Q^{-1})_{TASC}$, *will include losses due to the resonator geometry (Chapter 3. 3), losses caused by helium vapor damping (Chapter 3. 4). These will be compensated by the gain introduced through a stimulated condensation of helium atoms (Chapter 3. 5).*

The overall TASC losses can be presented in the following manner :

$$(Q^{-1})_{TASC} = Q_g{}^{-1} + Q_{vop}{}^{-1} - Q_c{}^{-1} \qquad (3.\ 6.\ 2)$$

For the designed third sound resonator with $Q_g = 10^5$ *and different values of helium film thickness they are plotted in Fig. 3. 6. 2 below. There are several operating regimes corresponding to the different values of input heater power. Just turning the power on to be 0.1 μW will enhance third sound resonance by twenty percent right away. Negative energy losses during TASC experiment will reflect the necessary condition for it self-oscillation.*

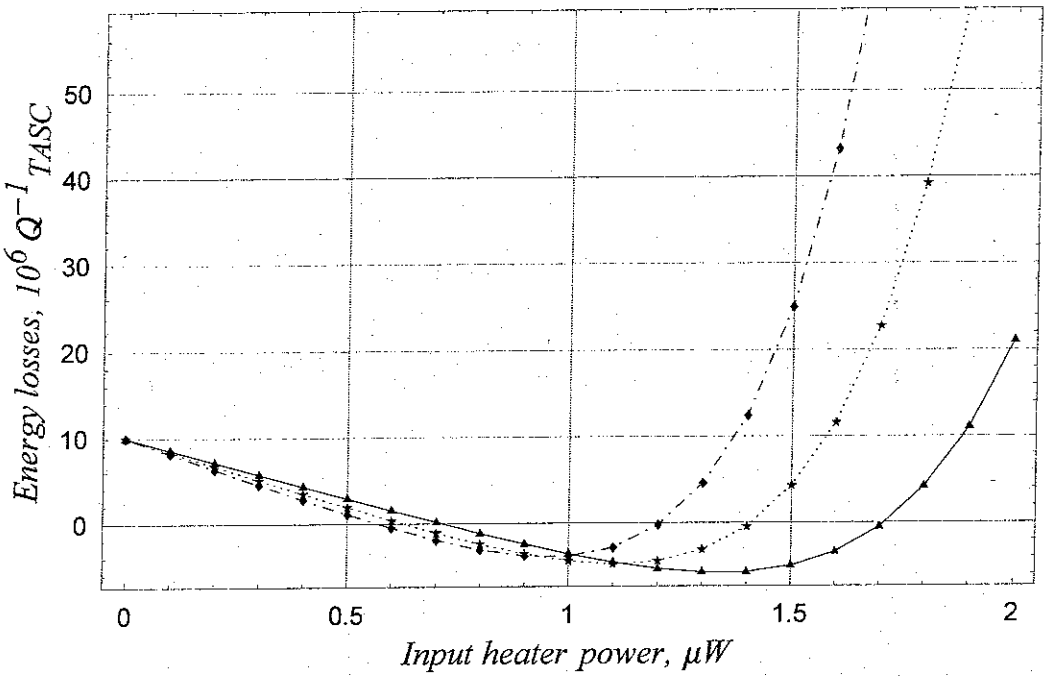

Figure 3. 6. 2. TASC observation as the heater power is turned on for the designed third sound resonator with $Q_g = 10^5$. Different point shapes correspond to different values of film thickness : triangle – 12, star – 16 and diamond – 20 layers.

It is clear from Fig. 3. 6. 2 that a critical input power for a self-oscillation will correspond to 0.7 μW, but a damping occurs already when this value is doubled.

It also might happen that for some reasons the actual value of the quality factor of third sound resonator is far from the targeted and calculated value of $Q_g = 10^5$.

Would it still be possible under these circumstances to observe the TASC effect? The answer is yes and it is supported by the Fig. 3. 6. 3 below provided that the practical resonator Q_g is at least around 10^4.

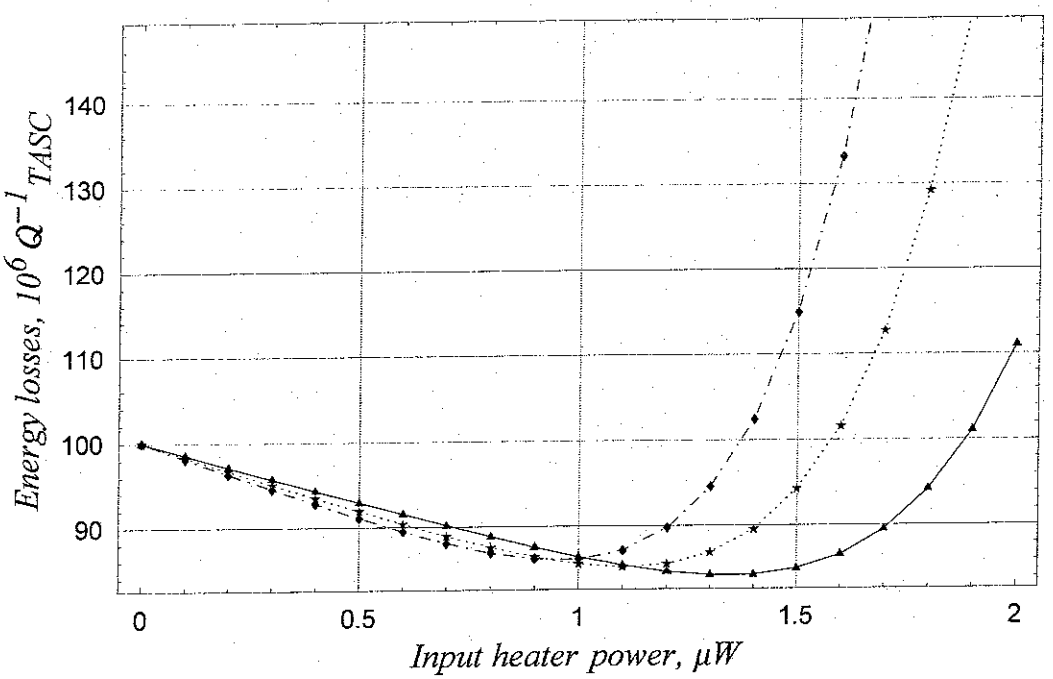

Figure 3. 6. 3. TASC observation as the heater power is turned on for some practical third sound resonator with $Q_g = 10^4$. Different point shapes correspond to different values of film thickness : triangle – 12, star – 16 and diamond – 20 layers.

In this case a self-oscillation will not occur (losses are positive) but a critical input power of 0.7 μW will be at least sufficient to observe a ten percent increase in the quality factor of the third sound resonance under right conditions.

Chapter 4. Apparatus Assembling

The constituent components of our third sound resonator and the way it was built are discussed in this chapter, along with the detection system details and the principal parts of the dilution refrigerator used in the experiment.

4.1 Third sound resonator

Once the third sound resonator design has been concluded, we started the process of its implementation. The main components of our resonator included a vapor source, sapphire disk, capacitor plate and the base with a central post.

A copper base of 27. 2 mm in diameter with a central post of 3 mm in length and 1. 2 mm in radius was manufactured in the machine shop together with four needed copper pins, each 5 mm long by 2 mm diameter (Fig. 2. 4. 1).

In the physics evaporation lab, sapphire disk of 13 mm in diameter and 0.5 mm in thickness was smoothly rotated between two sources of silver that was used to cover each disk surface by a 2000 Å thick layer of silver except a small spot in the middle. That spot was preserved to hold the disk and glue it later to the base.

A 15 mm square of quartz has served initially as a capacitor plate. It took some efforts to drill a hole in it, then cover the plate by a mask to evaporate silver at four designed locations to produce two drive and two pick-up electrodes.

The assembling process was painfully meticulous, and it required a strict se-

quence of tasks to be carried out precisely, purely and in time. One mistake in the long list (Appendix 4) of procedures could easily nevaluate all previous successful steps.

To facilitate the assembling, we made a jig to mount the base on one plate and position the centered disk on another before it was glued.

In the course of time, at least five resonators have been assembled and put into the cryostat to be tested. As it usually happens in the experimental physics, our first runs were unsuccessful but still important ones because they suggested what needed to be improved.

First of all, we replaced the quartz by a circuit board plate to better match the expansion coefficient of epoxy because its previous contact with quartz did not savive the cooling. To strengthen a glue joint between the disk and central post, we even made 1 mm deep cuts in the latter wich decreased the surface area of contact by a quarter and made the contact itself more flexible at low temperatures. Moreover, to ensure an electrical contact between them, we provided a rim about 0.1 mm high along the central post perimeter and filed out some portion of it to make sure that central post touches the silver coating on the disk in more than one place.

And finally, to maximize a precision in centering a sapphire disk with respect to central post and eliminate any obvious human error, we revised our jig and the whole assembling process and came to the conclusion that our technologically challenging adventure requires some professional involvement. Therefore, shortly after, the detailed blueprints (Appendix 3) were kindly produced by Mr. Boule and new jig and base with our improvements were manufactured for us by Mr. Widlansky in the machine shop.

Thus, we can go through the whole process of resonator assembling on a new

ground to meet the challenging resonator requirements for a succsessful TASC experiment. That process consists of three major activities : evaporation, gluing and mounting with specific details provided in Appendix 4. Here, they are outlined to get an idea.

A loop – shaped, about 9 mm diameter vapor source (Fig. 4. 1. 1) was made of thin wire with a 412 Ω resistance and small contraction coefficient at low temperatures.

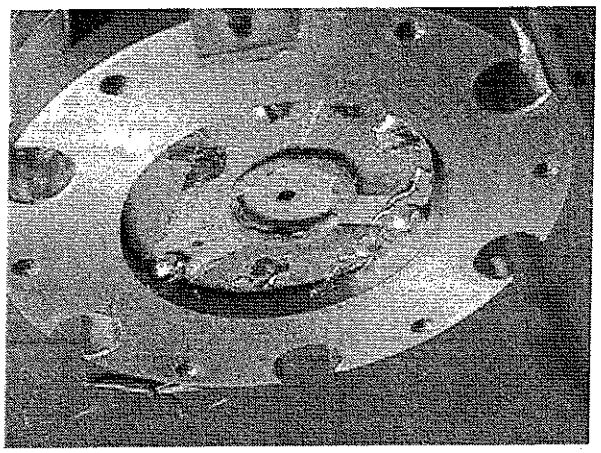

Figure 4. 1. 1. Made of the wire in a loop of 9 mm diameter, vapor source for the TASC experiment.

It was independently supported and centered 1. 3 mm above the sapphire disk coated on all surfaces with 2000 Å layer of evaporated silver. To get as uniform as possible the dik coverage, we made a rotor and placed it inside the evaporation chamber to be able to rotate sapphire disk during evaporation process.

Then sapphire disk was carefully placed in a specified position on a fixed lower jig and was held by the vacuum. It was barely covered by four 12 μm thick kapton film

spacer strips positioned diagonally on the same jig. A 12. 7 mm square of circuit board (Fig. 4. 1. 2) was used as a capacitor plate, hand polished very finely and lapped for flatness and divided into four segments to provide two couples of transducers – drives (D_1 and D_2) and pick-ups (P_1 and P_2), correspondingly, which is shown below.

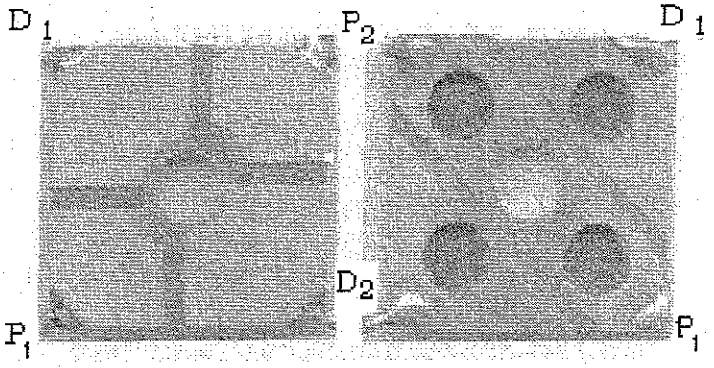

Figure 4. 1. 2. Capacitor plate to be used in the TASC experiment. Top side (on the left) is divided to provide a couple of drive and pick-up transducers connected as shown (on the right).

The board was also placed above the disk with spacers into a fixed position to prevent its rotation at the time of gluing the central post to that clean spot without silver in the middle of sapphire disk. A mixture of Easypoxy K – 45 and silver flakes was prepared to be viscous but not pastey. The upper jig carrying the base with central post was leveled and a tiny amount of mixed epoxy was transfered by a needle onto the small areas cut at the top of the central post without spilling over the rim.

With a pivot junction maintained by balls in the first jig (see Appendix 3), the

upper jig was lowered and central post made a firm contact with sapphire disk since two jigs were tightened slightly by a screw with a spring.

Another fresh and pure epoxy mixture was used to glue four pins to the bottom of circuit board (Fig. 4. 1. 2) and then more fluid Stycast 1266 epoxy was prepared to glue these pins to the base. We needed to press on the individual pins after gluing them to insure that the spacers lay flat and to provide the smallest capacitor gap achievable under given circumstances. For this reason, a light weight rested on the metal pins with springs was used.

After 24 hours, with a maximum care, the press was removed as well as spacers, jigs were separated and the base – dismounted from one of them. The whole process of resonator assembling was performed in an air filtered clean room available in the department.

The novel third sound resonator with 18 μm capacitor gap was cautiously transfered and fixed in the cryostat in the same room after being electrically checked again.

To make a total pick-up electrode insensitive to antisymmetric vibrations, the transducers P_1 and P_2 were electrically connected. But D_1 and D_2 transducers were kept separate for a possible rotational drive phasing.Then the four capacitances were measured to assure that proper spacing was achieved.

Bolted to the matching flange of Fig. 4. 1. 1, the first successful implementation of the third sound resonator is shown in Fig. 4. 1. 3.

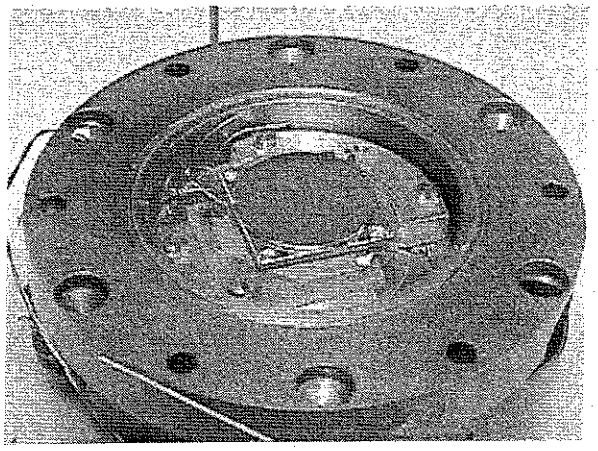

Figure 4. 1. 3. The first successful third sound resonator on early stages of the TASC.

▪ 4. 2 Detection System

The height oscillations of third sound wave in our experiment were detected capacitively [*4. 1*]. *We applied an alternating voltage up to 30* V_{pp} *to the drive electrodes* D_1 *and* D_2 (*Fig. 4. 1. 2*) *to excite the* (*2, 1*) *third sound mode in helium film.*

A change in the film thickness in the pick-up region corresponded to a capacitance modulation which was converted into an electric signal by implementing the pick-up capacitance into LC tunnel diode oscillator (*TDO*) *phase locked to a reference synthesizer* (*Fig. 4. 2. 1*).

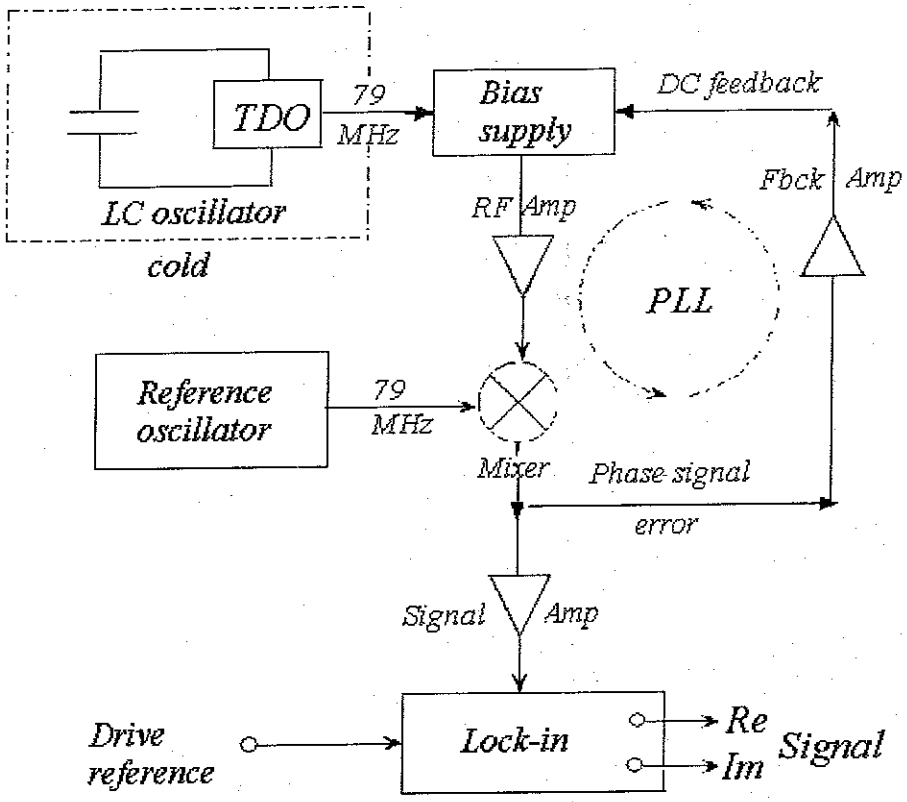

Figure 4. 2. 1. Detection system for the TASC experiment.

By comparing the TDO phase to a fixed reference oscillator, it was forced, through the feedback, to follow the reference phase. The control signal needed to accomplish this was proportional to the frequency changes which would have occurred without the feedback. The net result has appeared as a voltage proportional to the capacitance change.

A TDO cuircuit used in the lab and driven by BD – 7 tunnel diode is depicted in Fig. 4. 2. 2. The DC power is supplied by a room temperature current source which is connected to the circuit through the same coaxial cable that carries the small RF output signal from the TDO.

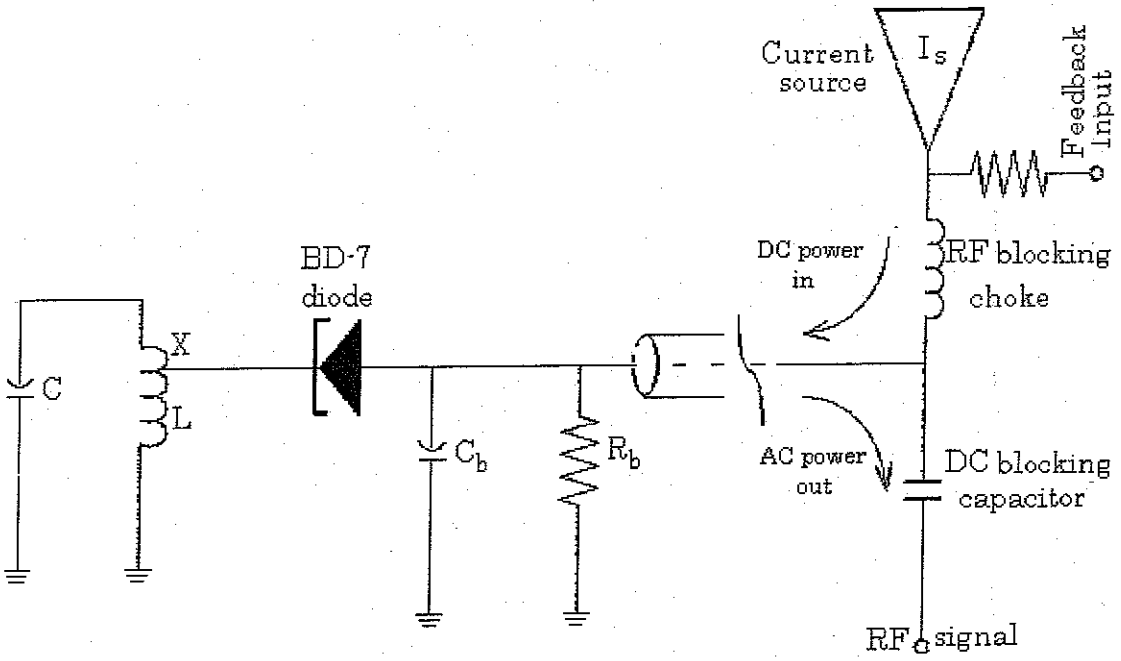

Figure 4. 2. 2. Schematic diagram of the TDO circuit with C = 15 pF, L = 0.37 μH, C_b = 300 pF, R_b = 6970 Ω, I_S = 13 μA, V_n = 64 mV.

The inductance L was chosen to give the disired operating frequency of the LC circuit. The tapping fraction X = 0. 8 of the coil was dictated by the impedance Z_0 of the LC circuit at the resonance. For the desired critical oscillation condition, the impedance across the tap, $Z_{tap} = X^2 Z_0$, must be slightly greater than effective negative resistance R_n [4. 2]. Since both Z_0 and R_n depend on temperature, their values were determined by size of "kink" region on the TDO I − V curves (Fig. 4. 2. 3) and adjusted, by varying X, to provide the disired amplitude of 69 MHz of frequency oscillation.

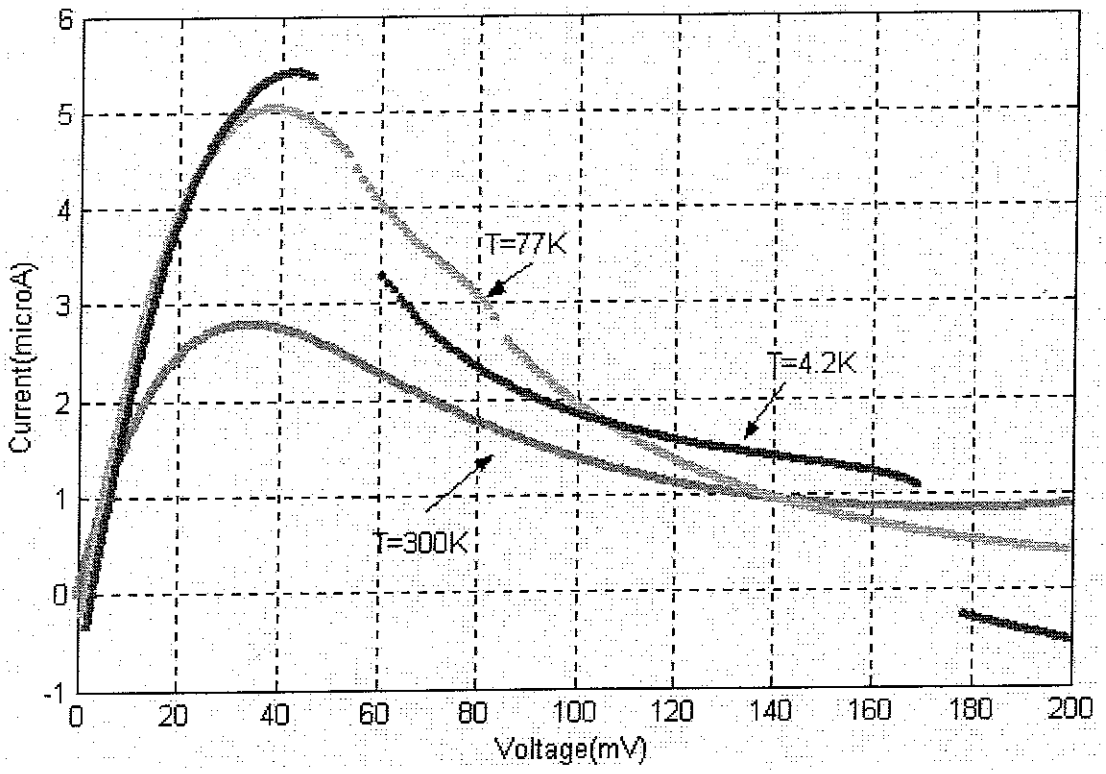

Figure 4. 2. 3. Experimental current – voltage characteristics of BD – 7 diode at three different temperatures. Oscillations are clearly pronounced at 4.2 K.

To accurately measure our signal frequency changes, we have employed the phase-locking technique (Fig. 4. 2. 1). The accuracy of this approach is limited mostly by the instability of both oscillators with one used as a reference signal. In order to minimize the error, a feed back signal from the mixer was sent directly to the TDO.

As a nonlinear circuit element, the mixer admits two input signals of frequencies f_{TDO} (from the TDO) and f_{OSC} (from the local reference oscillator) and outputs a signal which consists of both sum and difference of those two.

The sum frequency signal is eliminated and difference is amplified by passing through pre-amplifier 1, whose output is sent back to the TDO as a feed back. Since frequency of the TDO depends [4. 2] on the bias voltage, and a feed back signal propagates in the same cable line as the bias current, it slightly changes the bias voltage which causes the TDO frequency modulation. When a feed back signal cancels out frequency variations due to capacitance oscillations, the loop is said to be locked. The difference frequency is zero in this case, and the mixer acts as a phase comparator.

Pre-amplifier 2 was adjusted correspondingly to allow only those frequencies, which we were interested in, to be fed through a two phase lock-in amplifier, referenced to the output of the drive oscillator. The lock-in was set to monitor its input to a signal at twice the drive frequency. The amplitude of this signal was changing as we scanned the drive frequency through a resonance. And finally, the output of the lock-in amplifier was recorded by a computer.

▪ 4. 3 Dilution refrigerator

Our calculations (Chapter 3) suggested the experimental working temperature regime for the successful TASC experiment of 0.26 K. To achieve this temperature, a continuously operating dilution refrigerator (Fig. 4. 3. 1), assembled by Dr. Ellis some

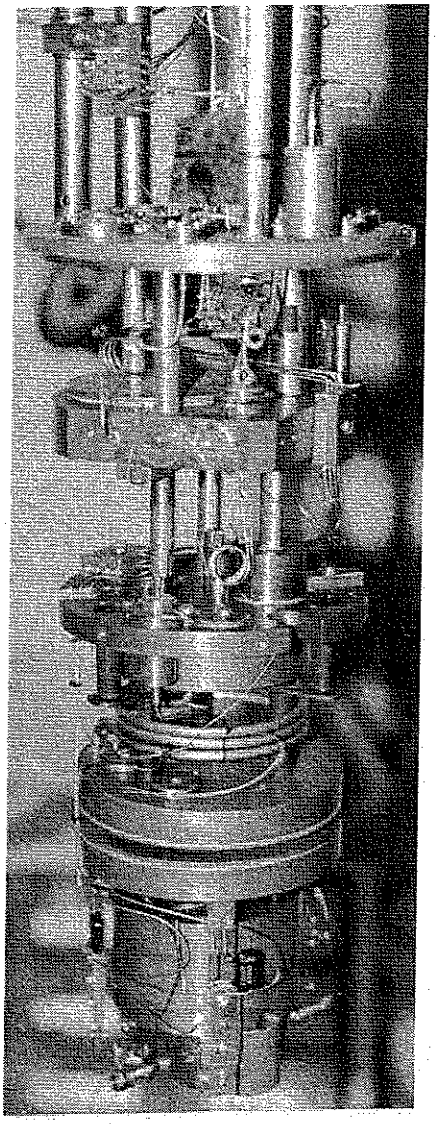

Figure 4. 3. 1. Dilution refrigerator for the TASC experiment.

time ago, has been employed in the lab.

The principal parts [3. 7] of this continuously operating dilution refrigerator are shown in Fig. 4. 3. 2. The phase separation occurs in the mixing chamber, and cooling is produced there by causing ^{3}He atoms from the upper, almost pure ^{3}He

phase to move across the boundary to the lower, dilute phase. The continuous dissolution of ^{3}He atoms from the concentrated to the dilute phase is obtained by circulating ^{3}He in the system by means of a pump at room temperature.

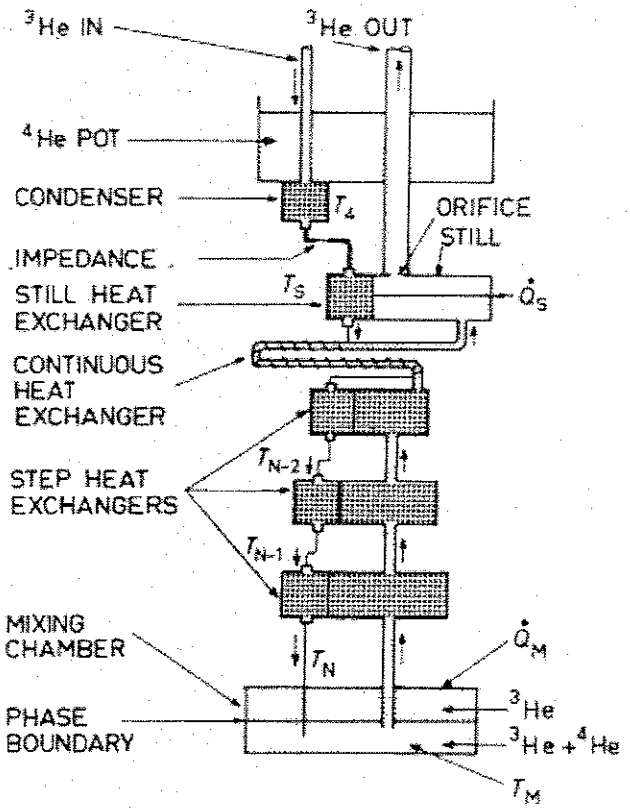

Figure 4. 3. 2. The principal parts of our dilution refrigerator (after [3. 7]). The external heat leaks to the still and the mixing chamber are denoted by $\dot{Q}_S$ and $\dot{Q}_M$.

Incoming helium gas is first precooled and liquefied in the condenser attached to the ^{4}He pot at about $T_4 = 1.6$ K. This temperature is reached by a pumping on ^{4}He pot as well. The pressure of ^{3}He is kept sufficiently high for condensation to occur by means of a flow impedance [4. 3]. The liquid then enters the still heat exchanger at T_S (about 0.7 K), the continuous exchanger, the step exchangers, and finally the mixing chamber. After crossing the phase boundary, ^{3}He atoms, driven by an osmotic pressure gradient, proceed through the heat exchangers to the still. Vapor from the still is removed by pumping on it. We also apply some external heating to the still in order to get a sufficient gas circulation rate.

As a circulation of ^{3}He in the system goes on, the temperature of the mixing chamber reduces down to the required values for our experiment. The experimental cell chamber (Fig. 4. 1. 3) containing the third sound resonator was attached to the mixing chamber and a good thermal contact was established between them.

The temperature was measured by carbon resistors calibrated with a ^{3}He melting curve thermometer and regulated by a heater in the cell chamber.

Chapter 5. Experimental Results

The first third sound experimental data on a novel resonator have been presented and values of the quality factor for our third sound resonance with a heater power "on" and "off" were analysed to make a conclusion about TASC effect detection.

5.1 Liquid nitrogen temperature data

Once we understood, after reaching liquid nitrogen temperature of $T = 77\ K$, that TDO started to oscillate (Fig. 4. 2. 3) reliably at a frequency $f_{TDO} = 79.5\ MHz$, we began to explore the mechanical stability of third sound resonator to be sure that its glue connections savived the cooling process. For this reason, we applied voltage that was less than 1 V_{p-p} to both drives and recorded the responce of our resonator to the driving frequency that was scanned in the whole range from 100 Hz to 20 kHz.

From the previous experiments [5. 2] we have learned that there are three pronounced mechanical resonances associated with a proposed third sound resonator design. At that point, it was not clear what kind of resonator motions they might correspond to. But their presence has proved to be a consistent indicator that our resonator was still in a good shape. We were stunned, of course, by the appearence of a huge peak around 1.1 kHz but decided to go forward, anyway.

The first mechanical resonance was observed at a frequency $f_1 = 5113.42\ Hz$

(Fig. 5. 1. 1) and had a quality factor $Q_1 = 1119$ determined by a fitting procedure.

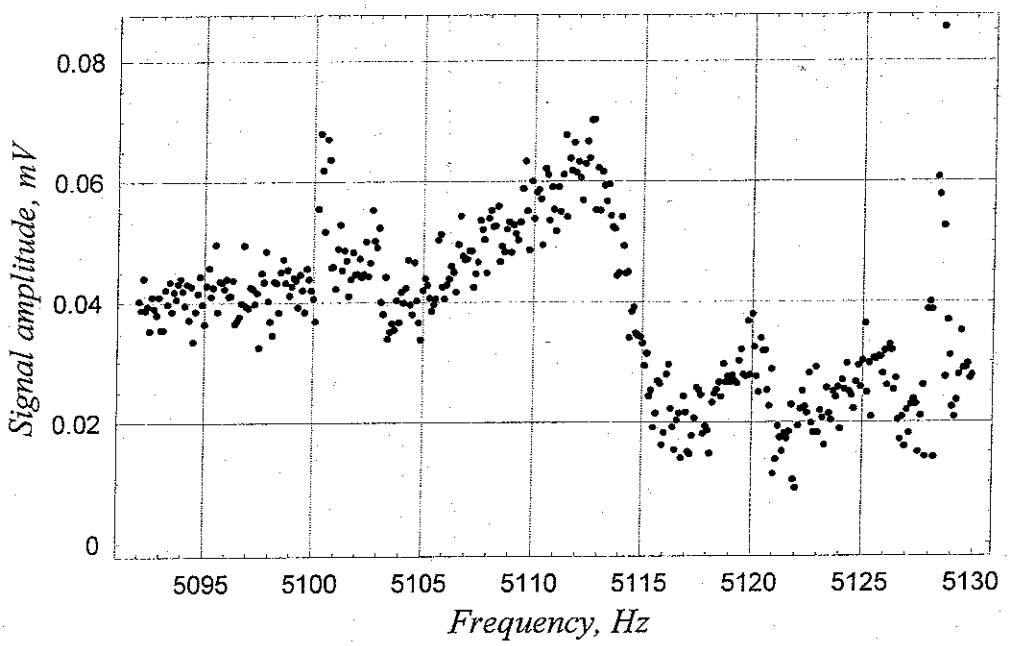

Figure 5. 1. 1. Mechanical resonance at 5113.42 Hz.

We observe from Fig. 5. 1. 1 that a signal background was quite noisy for that scan which had implied that we needed more time to spend on taking each experimental data point.

That was corrected on the next scan when getting second mecanical resonance (Fig. 5. 1. 2) at a frequency $f_2 = 6754.51$ Hz and $Q_2 = 447$. This time we averaged each point longer and substantially reduced the noise.

Third mechanical resonance (Fig. 5. 1. 3) at a frequency $f_3 = 12478.5$ Hz and $Q_3 = 729$ always appears to be the largest and least noisy one.

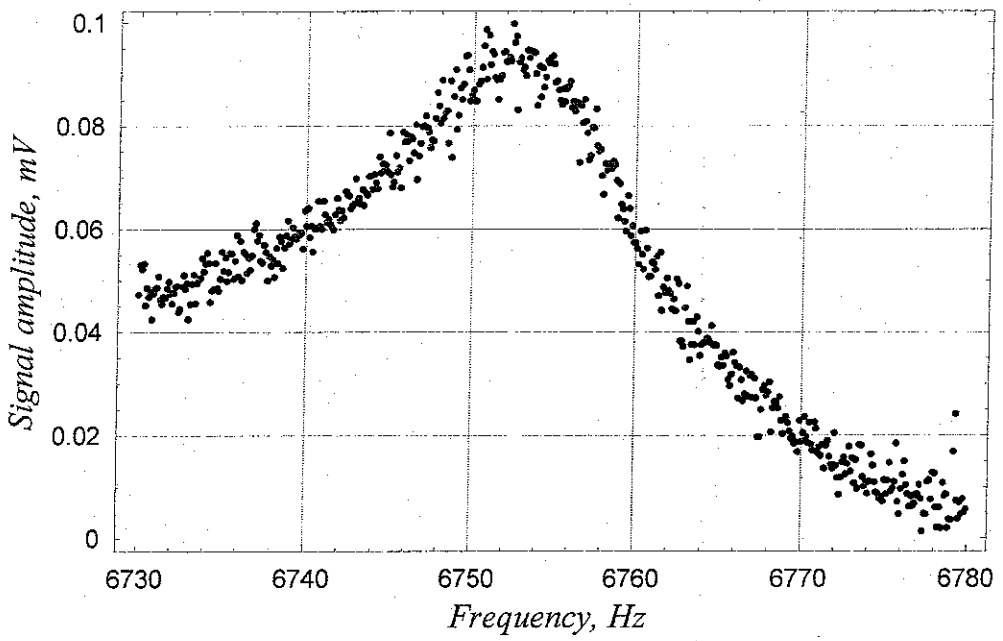

Figure 5. 1. 2. Mechanical resonance at 6754.51 Hz.

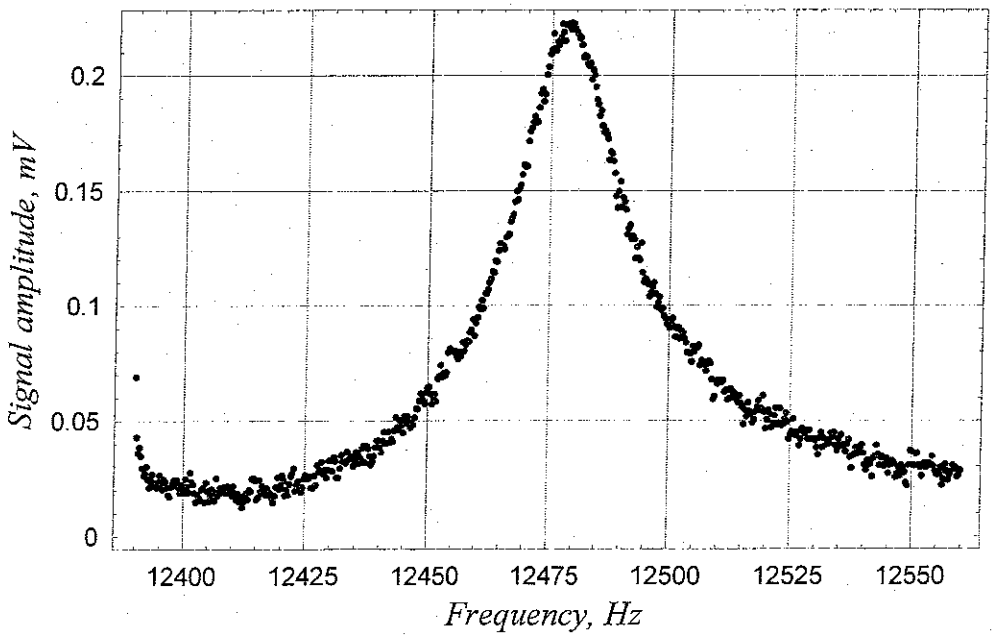

Figure 5. 1. 3. Mechanical resonance at 12478.5 Hz

▪ 5. 2 Superfluid helium temperature data

Since our first ultimate goal was to observe the third sound resonance, we continued lowering temperature further until we reached $T = 0.3\ K$. Unfortunately, background noise due to unexpected presence of 1.1 kHz peak limited our sensitivity tremendously. Nevertheless, we made some adjustments to the detection system to reduce a background to 150 μV at 5 V_{p-p} drive voltage. Despite our low sensitivity of 1 mV at the background signal of 420 μV and signal amplitude around 0.2 mV, we kept our search for the third sound which we estimated was to resonate between 300 Hz and 400 Hz for an approximate speed $c_3 = 10\ m/sec$ of the third sound wave.

In the long run, our persistence was praised (Fig. 5. 2. 1) by the observation of

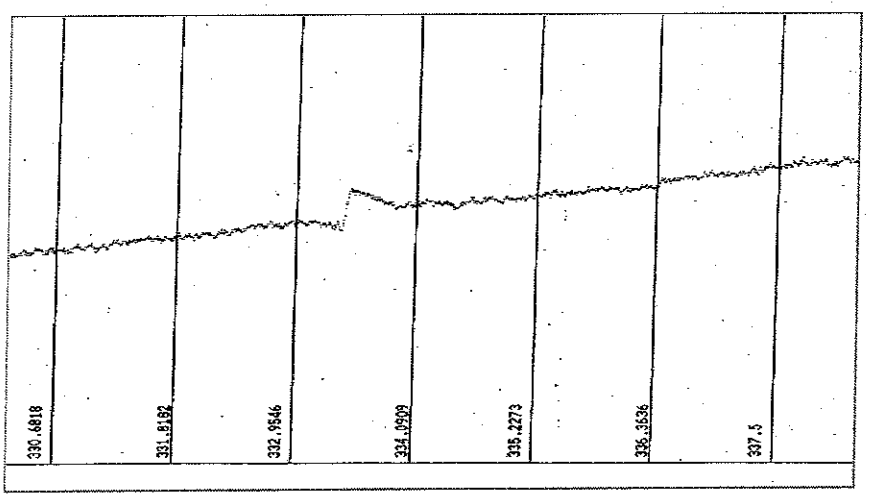

Figure 5. 2. 1. Third sound signal observed on a chartrecorder.

our first third sound resonance on a newly designed resonator. Though relatively small, it was a signal we were waiting for a quite some time after many trials, tests and runs.

With a 5 V_{p-p} drive voltage we slowly scanned through the resonance many times recording by a computer the real and imaginary parts of a signal at the output of our lock-in amplifier.

To get precise values of the resonance frequency f_o of our third sound and its quality factor Q_{TASC} as well as a scaled amplitude A_o along with its phase ϕ, we used a least square fit routine to analyse the data by means of the formula (5.2. 1) that was a solution in a frequency domain [5. 2] to the differential equation describing the motion of a slightly damped, driven harmonic oscillator.

$$\mathcal{A}(f,\ f_o,\ Q_{TASC},\ A_o,\ \phi) = \frac{A_o\, e^{i\phi}}{Q_{TASC}\left[1-\left(\frac{f}{f_o}\right)^2\right]+i\,\frac{f}{f_o}} \qquad (5.2.1)$$

It appeared that the best quality third sound resonance (Fig. 5. 2. 2) took place at the frequency f_o = 333.58 Hz and had a quality factor of 4268, which was much smaller than the value employed in our theoretical modeling (Chapter 3) and anticipated to characterize the third sound resonance for the successful TASC observation.

Nevertheless, we scanned through the resonance over fifty times, at least, driving it with 5 then 6 V_{p-p} voltage with a heater power "on" and "off" to collect as much data as we could. To provide 1 μW of power to the resonance, we sent 50 μA dc current through the heater wire.

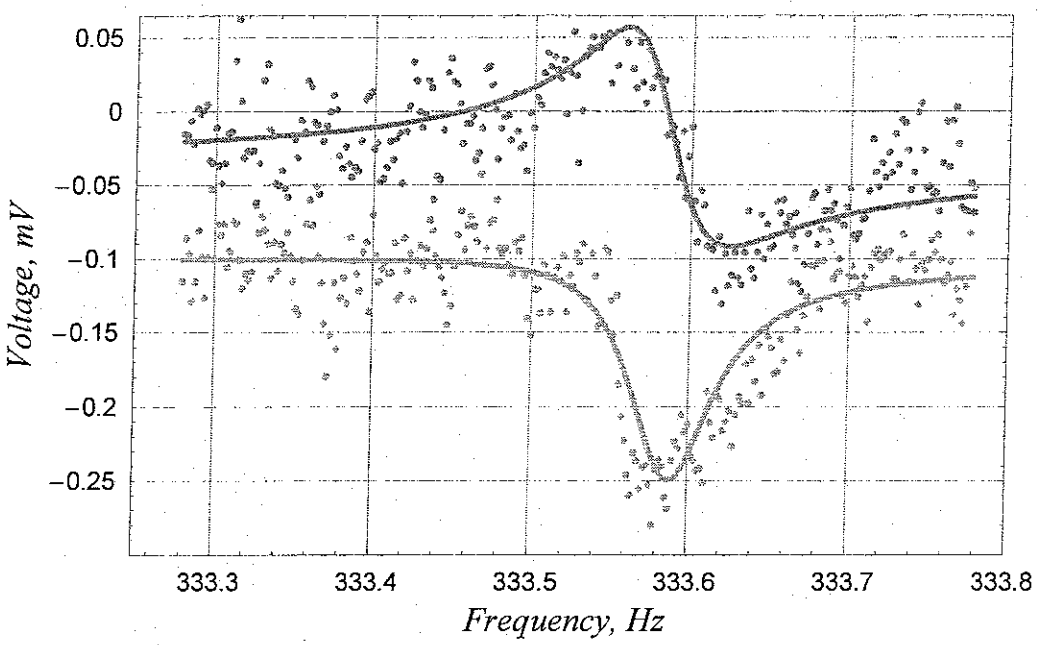

Figure 5. 2. 2. Real (green) and imaginary (red) parts of the third sound signal amplitude. Dots represent the experimental data and lines – their fit.

Then values of Q were extracted for each of the runs with the heater power "on" to be compared with those results obtained without a heater source (Fig. 5. 2. 3).

At this point, we shoud not get discouraged by the outcome of the experiment since it signals what actually happened. As we observe from Fig. 5. 2. 3, there is a frequency shift of 0.1 Hz between two data sets which means that values of Q for the runs with a heater power "on" corresponded to a higher helium film temperature than that we started with when a heater power was "off". This conclusion is supported by the dispersion relation for the third sound, formula (2. 1. 6), and the relative density, ρ_S / ρ_n, temperature dependence (Fig. 1. 3. 1) determining the third sound speed, c_3, as a function of temperature.

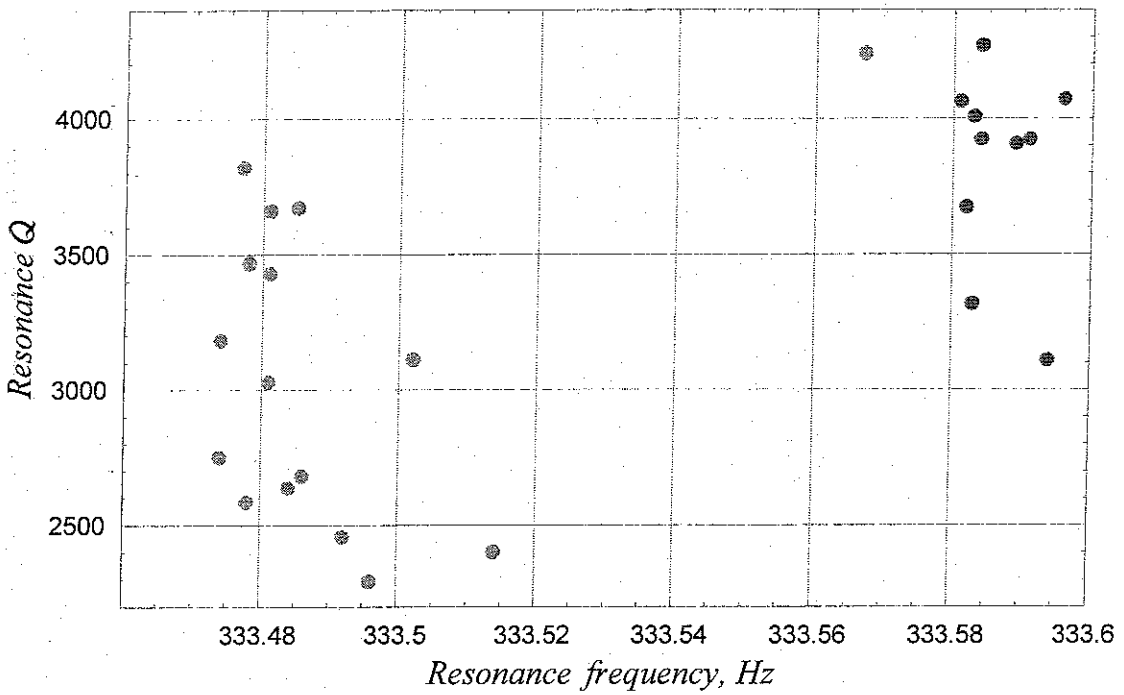

Figure 5. 2. 3. Resonance values of Q for 5 V_{p-p} drive with a heater power "off" (blue) and heater power of 1 μW "on" (red).

It appeared that by sending 1 μW of power into the third sound resonance at the initial film temperature of 0.3 K, we overheated the film significantly to reach 0.57 K, (in correspondence to 0.1 Hz resonance frequency shift), which was twice as higher of the working temperature limit. This was apparently due to a poor thermal contact that was induced by a cracked glue joint between sapphire disk and a central post of copper base. It also might explain the presence of 1.1 kHz peak and low quality factor values of the mechanical resonances at nitrogen temperature.

Thus, a broken third sound resonator prevented us to observe an increase in

Q after a heater power was turned on. For the given averaged value of $Q = 3826$ (Fig. 5. 2. 3) with the standard deviation $\sigma = 360$ that increase was estimated to be 154 and could still be observed with a resolution of 114 for these ten data points.

Therefore, to answer the ultimate question about the TASC phenomenon, we definitely need to meet the all neccessary requirements on the third sound resonator which will assure the high quality third sound resonance and provide an unequivocal evidence on the third sound amplification by stimulated condensation of helium atoms into the resonating third sound mode.

▪ Conclusion

In the process of quantum condensation helium atoms from the vapor become affiliated with the velocity field of a persistent current circulation state. As a result, the superfluid component absorbs the mass, and the excitations, making up the normal component, account for the energy and momentum of the condensing atom.

Condensing atoms will be assimilated into the macroscopic flow velocity state of the third sound mode since the flow field of the wave, on the time and size scale of the condensing event, is indistinguishable from that of a persistent current.

Superfluid mass can be removed from a third sound resonance of a non − zero angular momentum state by DC film flow, preserving the AC energy in the third sound mode. This will result in a gain that should be observed (Fig. 3. 6. 2 − 3) as an increase in the quality factor Q_{TASC} of the third sound resonance as a non − equilibrium flux of vapor atoms is condensed into the film.

In order to detect third sound amplification due to stimulated condensation of helium vapor atoms into a resonating (2, 1) mode, third sound resonator must satisfy strict requirements [2. 9]. Experimental data (Fig. 5. 2. 2), obtained on the proposed in this thesis a novel resonator, support the conclusion that there is no obvious obstacle for the successful discovery of the TASC phenomenon.

▪ Appendix 1

I was provided with some theoretical data (Fig. A1. 1) on helium film specific heat C (T, d) and third sound (Fig. A1. 2) quality factor Q_0 (T, d) temperature dependencies for a particular helium film thickness in the number of layers d.

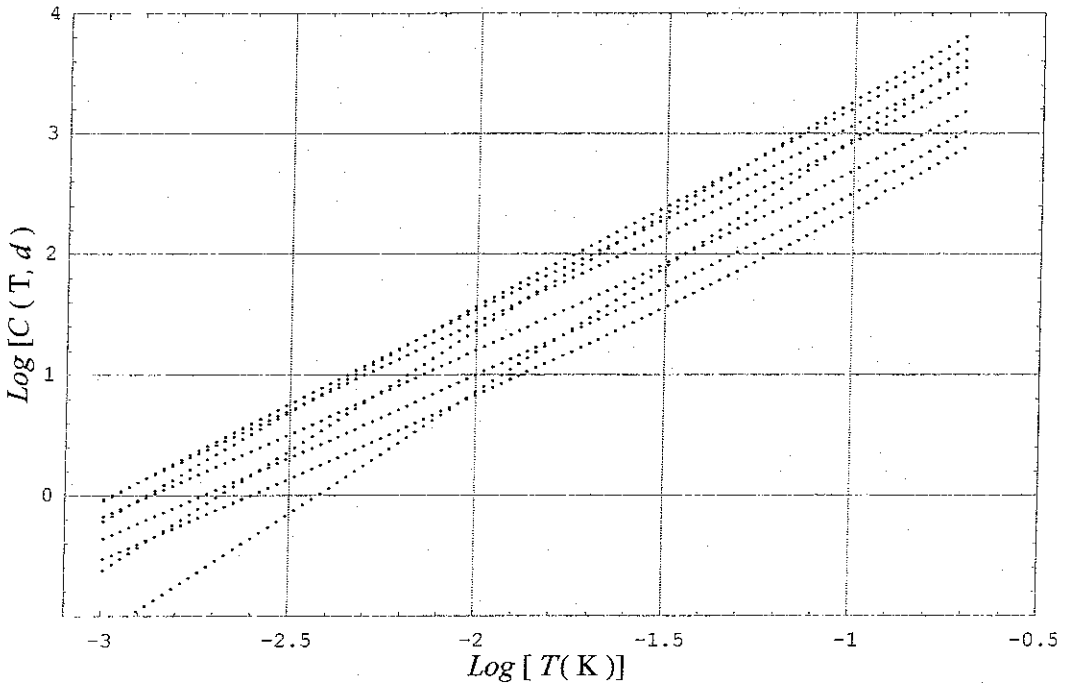

Figure A1. 1. Scaled helium film specific heat theoretical data. Film thickness is reflected by the number of layers d in the figure.

Each specific heat and quality factor data sets with a given d were fitted to the following

$$Log\,[C] = \frac{2\,(x-\alpha)\,(x-\alpha)^2+\beta}{(x-\alpha)^2+\delta} + \gamma \qquad (A1.\ 1)$$

$$Log\left[c_3\,Q_o^{-1}\right] = A + Bx - \frac{1}{x-C} \qquad (A1.\ 2)$$

expressions, correspondingly, where $x \equiv Log\,[T]$.

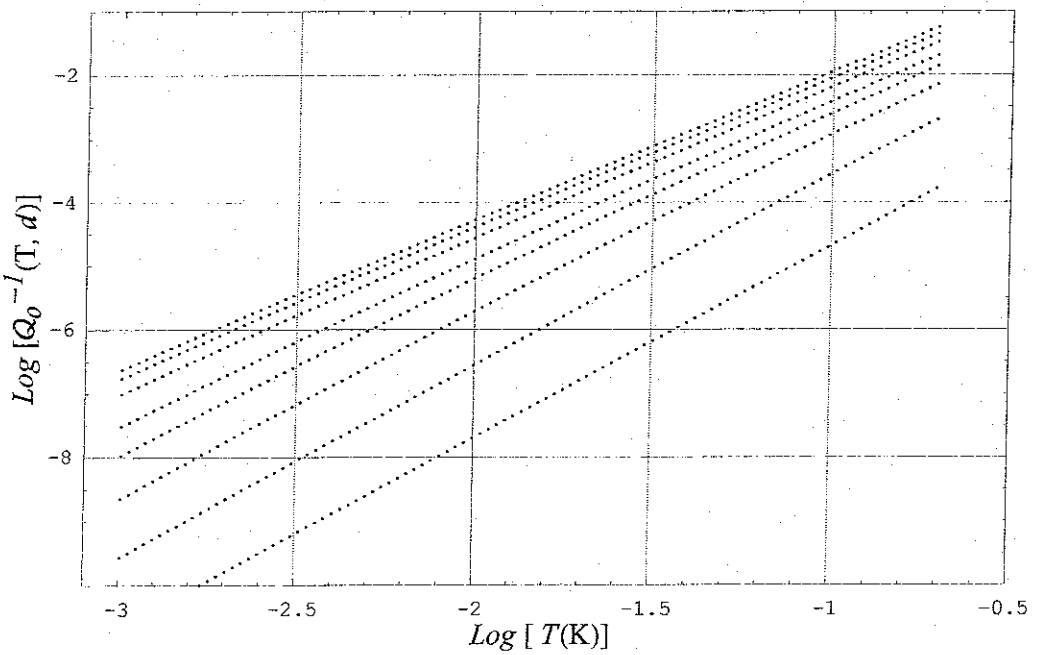

Figure A1. 2. Third sound quality factor theoretical data. Film thickness is reflected by the number of layers d in the figure.

Thus, we recieved as many sets (for each value of d) as the total number of coefficients involved in equations (A1. 1 – 2). By fitting them in turn, we get analitycal forms

$$\alpha[d] = -2.5938 + 5.4088\, e^{-0.3796\, d} \qquad (A1.\ 3)$$

$$\beta[d] = 23.1931\, Exp\left[-0.1035\, d - \frac{32.6124}{d^{2.4802}}\right] \qquad (A1.\ 4)$$

$$\gamma[d] = -0.1198 + 8.7995\, e^{-0.296\, d} \qquad (A1.\ 5)$$

$$\delta[d] = 41.0192\, Exp\left[-0.1143\, d - \frac{28.8123}{d^{2.1967}}\right] \qquad (A1.\ 6)$$

$$A[d] = 0.06256 + 0.0381\, d - \frac{52.904}{d^{4.0953}} \qquad (A1.\ 7)$$

$$B[d] = 2.2807 + 4.4372\, e^{-0.6256\, d} \qquad (A1.\ 8)$$

$$C[d] = -2.4574\, Exp\left[0.0889\, d + \frac{36.5438}{d^{3.6496}}\right] \qquad (A1.\ 9)$$

which after substitution them into equations (A1. 1 – 2) will provide us with functional dependencies $C[T,\ d]$ *and* $Q_o^{-1}[T,\ d]$ *to be emploed in equations (3. 4. 7 – 8).*

Appendix 2

An outline of the major steps in theoretical modeling (Chapter 3) which led to the expression for the magnitude of the critical quality factor Q_C, equation (3. 5.7), that reflects a balance between energy input into third sound mode and dissipation of the latter.

$$\mathcal{F}(\chi, \zeta, \rho) = \frac{\dot{\mathcal{N}}}{a^2}\,\Phi(\chi, \zeta, \rho), \qquad (3.\,1.\,6)$$

where

$$\Phi(\chi, \zeta, \rho) = \frac{\zeta}{8\pi^2}\,\frac{2\pi\;{}_2F_1\left[1.25,\ 0.75;\ 1;\ u^2\right]}{(\chi^2+\zeta^2+\rho^2)^{1.5}} \qquad (3.\,1.\,7)$$

$$\mathcal{P}_{ac} = \int_{disk} \mathcal{F} \prec \frac{m_4 v^2}{2} \succ_{\mathcal{T}} d\mathcal{A} \qquad (3.\,5.\,1)$$

$$\mathcal{P}_{dc} = \int_{disk} \mathcal{F}\,\mathcal{L}\,k_b\,d\mathcal{A} \qquad (3.\,5.\,2)$$

$$\eta(r,\ \phi,\ t) = \eta_0\,J_m(k_{mn}\,r)\cos(m\phi)\cos(\omega_{mn}\,t) \qquad (A2.\,1)$$

$$\frac{\partial}{\partial r}J_m(k_{mn}\,r) = \frac{\partial}{\partial r}J_m(u) = \frac{\partial}{\partial u}\,\frac{\partial u}{\partial r}\,J_m(u) =$$

$$= k_{mn} \frac{\partial}{\partial u} J_m(u) = k_{mn} J'_m(u) \equiv k J'_m(u) \qquad (A2.\ 2)$$

$$\vec{\nabla} = \frac{\partial}{\partial r} \hat{r} + \frac{1}{r} \frac{\partial}{\partial \phi} \hat{\phi} + \frac{\partial}{\partial z} \hat{z} \qquad (A2.\ 3)$$

$$\vec{\nabla} \eta = \eta_0 \cos(\omega t) \left[k J'_m(u) \cos(m\phi) \hat{r} - \frac{m}{r} J_m(u) \sin(m\phi) \hat{\phi} \right] \qquad (A2.\ 4)$$

$$\frac{\partial v_s}{\partial t} = -g \nabla h \qquad (2.\ 1.\ 3)$$

$$\dot{v} = -g \vec{\nabla} \eta \qquad (A2.\ 5)$$

$$v(r) = \frac{-g \eta_0}{\omega} *$$

$$* \left[k J'_m(u) \cos(m\phi) \sin(\omega t) \hat{r} - \frac{m}{r} J_m(u) \sin(m\phi) \sin(\omega t) \hat{\phi} \right] \qquad (A2.\ 6)$$

$$v^2 = \frac{g^2 {\eta_0}^2}{\omega^2} *$$

$$\left[k^2 {J'_m}^2(u) \cos^2(m\phi) \sin^2(\omega t) + \frac{m^2}{r^2} {J_m}^2(u) \sin^2(m\phi) \sin^2(\omega t) \right] \qquad (A2.\ 7)$$

$$< v^2 >_{\mathcal{T}} =$$

$$= \frac{g^2 \eta_o^2}{2 \omega^2} \left[k^2 J'_m{}^2(u) \cos^2(m\phi) + \frac{m^2}{r^2} J_m{}^2(u) \sin^2(m\phi) \right] \qquad (A2.8)$$

$$\int d\mathcal{A} = \int_0^a r\, dr \int_0^{2\pi} d\phi \qquad (A2.8)$$

$$\mathcal{P}_{ac} = \frac{\pi g^2 \eta_o^2 m_4}{4 \omega^2} \int_0^a \mathcal{F} \left[k^2 J'_m{}^2(u) + \frac{m^2}{r^2} J_m{}^2(u) \right] r\, dr \qquad (A2.10)$$

$$c_3{}^2 = g h_o;\ \omega_{mn} = c_3 k = c_3 x_{mn}/a \qquad (A2.11)$$

$$\chi = r/a \qquad \rho = \mathcal{R}/a \qquad \zeta = z/a \qquad (3.1.3)$$

$$\mathcal{P}_{ac} = \frac{\pi m_4 c_3{}^2}{4} \left(\frac{\eta_o}{h_o} \right)^2 a^2 *$$

$$* \int_0^1 \mathcal{F} \left[J'_m{}^2(x_{mn}\chi) + \left(\frac{m\, J_m(\chi\, x_{mn})}{\chi\, x_{mn}} \right)^2 \right] \chi\, d\chi \qquad (A2.12)$$

$$\mathcal{P}_{ac} = \frac{\dot{\mathcal{N}}}{4} \pi m_4 c_3{}^2 \left(\frac{\eta_o}{h_o} \right)^2 L_{mn}(\zeta,\ \rho), \qquad (A2.13)$$

where

$$L_{mn}(\zeta,\ \rho) \equiv \int_0^1 \Phi(\chi,\ \zeta,\ \rho)\left[J'_m{}^2(x_{mn}\,\chi) + \left(\frac{m\ J_m(\chi\,x_{mn})}{\chi\,x_{mn}}\right)^2\right]\chi\,d\chi$$

$$\mathcal{P}_{dc} = \int_{disk} \mathcal{F}\,\mathcal{L}\,k_b\,d\mathcal{A} = 2\pi\,\mathcal{L}\,\kappa_b\,\dot{\mathcal{N}}\,f(\zeta,\ \rho), \qquad (A2.\ 14)$$

where

$$f(\zeta,\ \rho) = \int_0^1 \Phi(\chi,\ \zeta,\ \rho)\,\chi\,d\chi \qquad (A2.\ 15)$$

But

$$\mathcal{W} = \mathcal{L}\,\kappa_b\,\dot{\mathcal{N}} \qquad (A2.\ 16)$$

Therefore,

$$\mathcal{P}_{dc} = 2\pi\,f(\zeta,\ \rho)\,\mathcal{W} \qquad (A2.\ 17)$$

To find the optimal heater parameters, we need to maximize the ratio $\mathcal{P}_{ac}\ /\ \mathcal{P}_{dc}$ *which for the* $(2,\ 1)$ *third sound mode of interest*

$$\frac{\mathcal{P}_{ac}}{\mathcal{P}_{dc}} \sim \frac{L_{21}(\zeta,\ \rho)}{f(\zeta,\ \rho)} \qquad (A2.\ 18)$$

will provide pairs of $(\zeta,\ \rho)$ *ploted in Fig. 3. 5. 1 with the optimal values of* $(\zeta,\ \rho)$ *to be* $(0.2,\ 0.66)$.

Critical values of Q *to sustain third sound oscillations can be found from*

$$Q_c = \omega_{mn}\,\frac{\mathcal{E}_{res}}{\mathcal{P}_{ac}} \qquad (3.\ 5.\ 6)$$

$$\mathcal{E}_{res} = \frac{\pi a^2}{x_m^2} c_3^2 \left(\frac{A}{h_o}\right)^2 \rho h_o J^2_{rms}, \qquad (3.3.5)$$

$$J^2_{rms} \equiv \frac{1}{2}\left(x_m^2 - m^2\right) J_m^2(x_m) \qquad (3.3.6)$$

$$h_o = h_1 * \left(\frac{3 \kappa_b T_v}{m_4 c_3^2}\right)^{\frac{1}{3}} \qquad (A2.19)$$

Making use of equations (A2. 11), (A2. 13), (A2. 16) with numerical parameters for the (2, 1) mode such as

$a = 0.0065\,(m)$; $m_4 = 6.7 * 10^{-27}\,(kg)$; $T_V = 40\,(K)$; $\rho = 145\left(kg/m^3\right)$;

$h_1 = 3.6 * 10^{-10}\,(m)$; $\kappa_b = 1.38 * 10^{-23}\,(J/K)$; $\mathcal{L} = 7.16\,(K)$;

$x_{21} = 3.05424$; $L_{21}(0.2,\ 0.66) = 0.00846.$

we arrive at

$$Q_c = \frac{4\,\omega_{21}/k_{21}^2\,\rho h_o J^2_{rms}(x_{21})}{m_4 L_{21}(0.2,\ 0.66)} \frac{\mathcal{L} \kappa_b}{\mathcal{W}} \qquad (A2.20)$$

which after numerical evaluation becomes

$$Q_c = 0.0307 \frac{\sqrt[3]{c_3^2}}{\mathcal{W}} \qquad (A2.21)$$

▪ *Appendix 3*

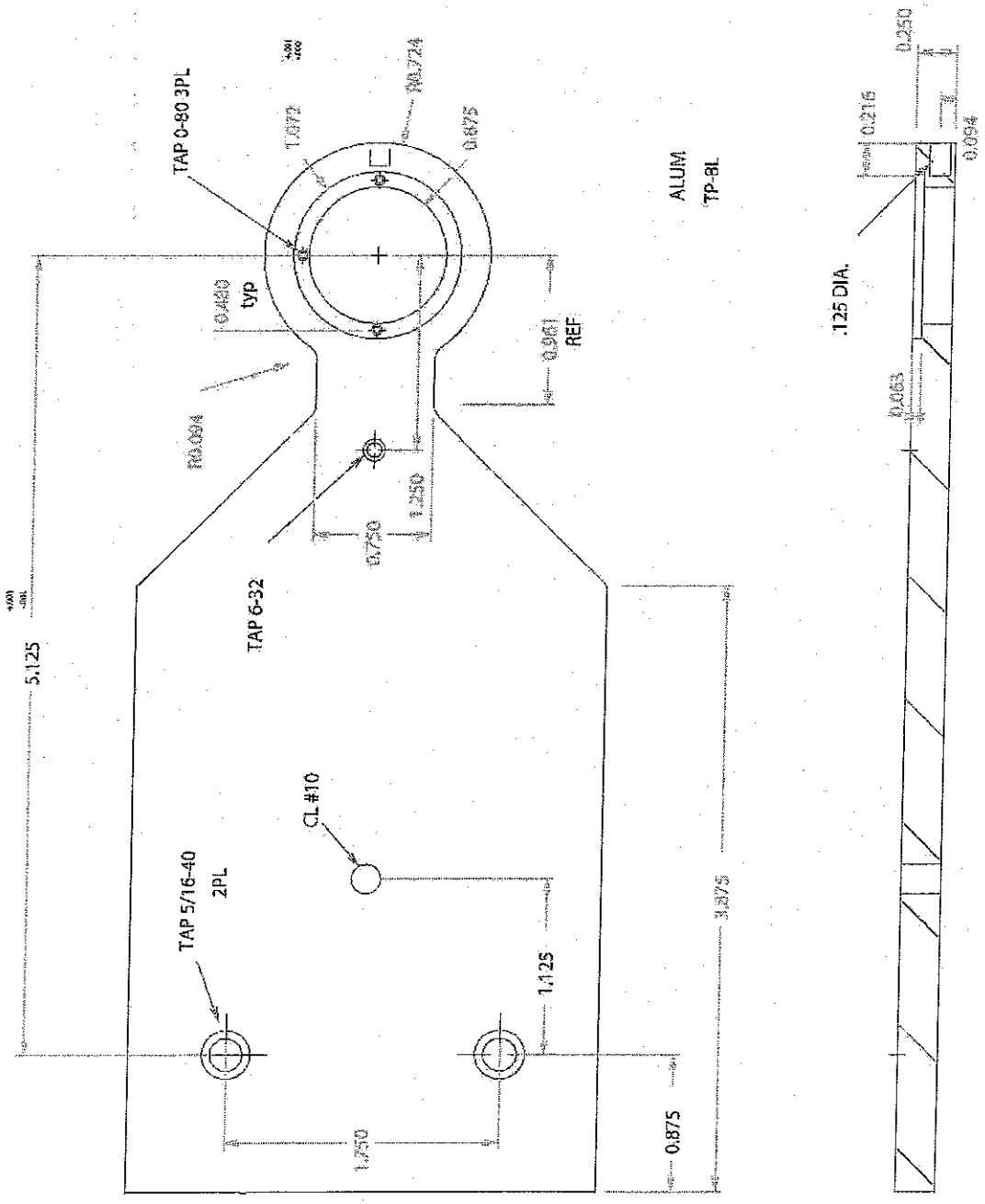

Figure A3. 1. The upper jig blueprint.

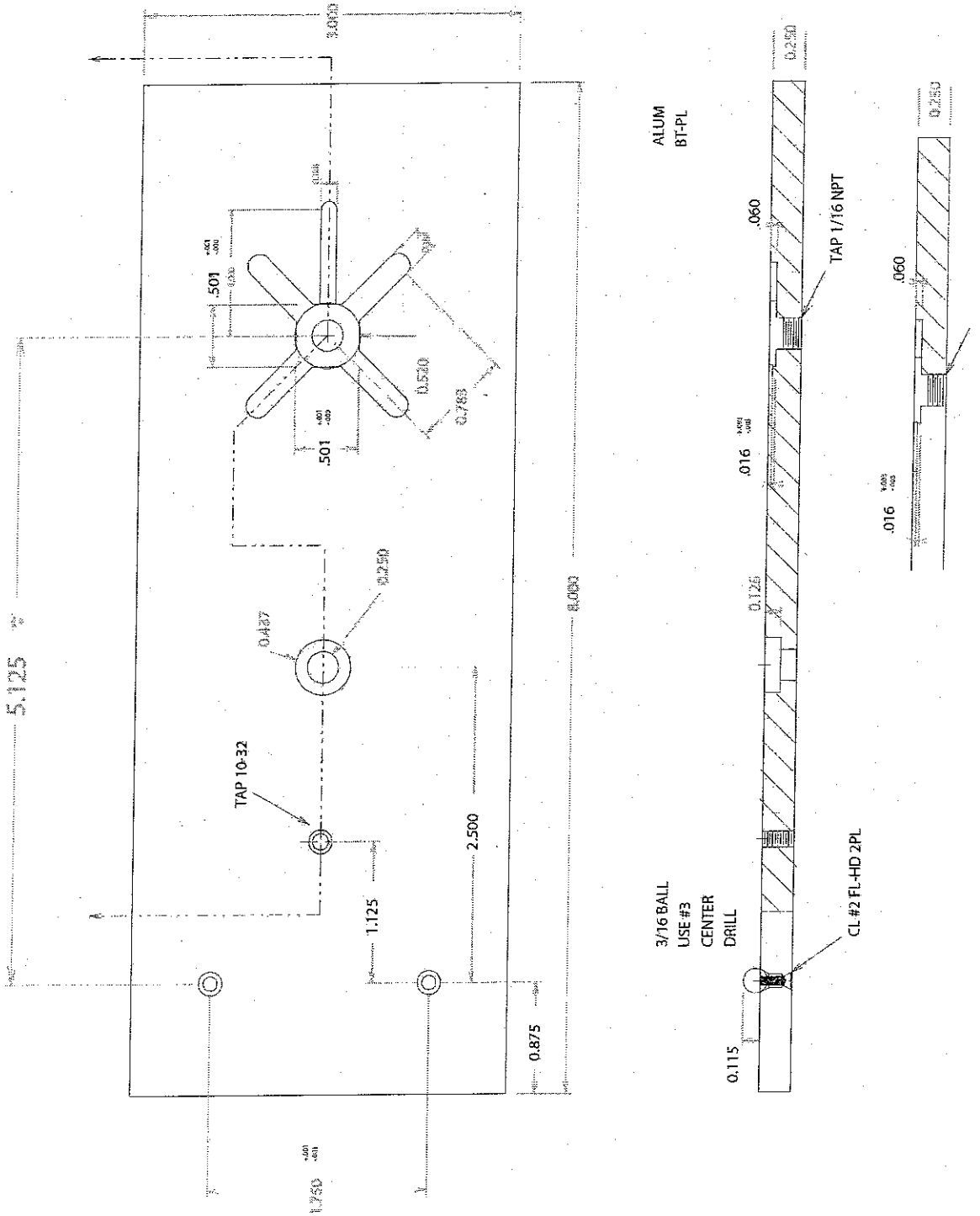

Figure A3. 2. The lower jig blueprint

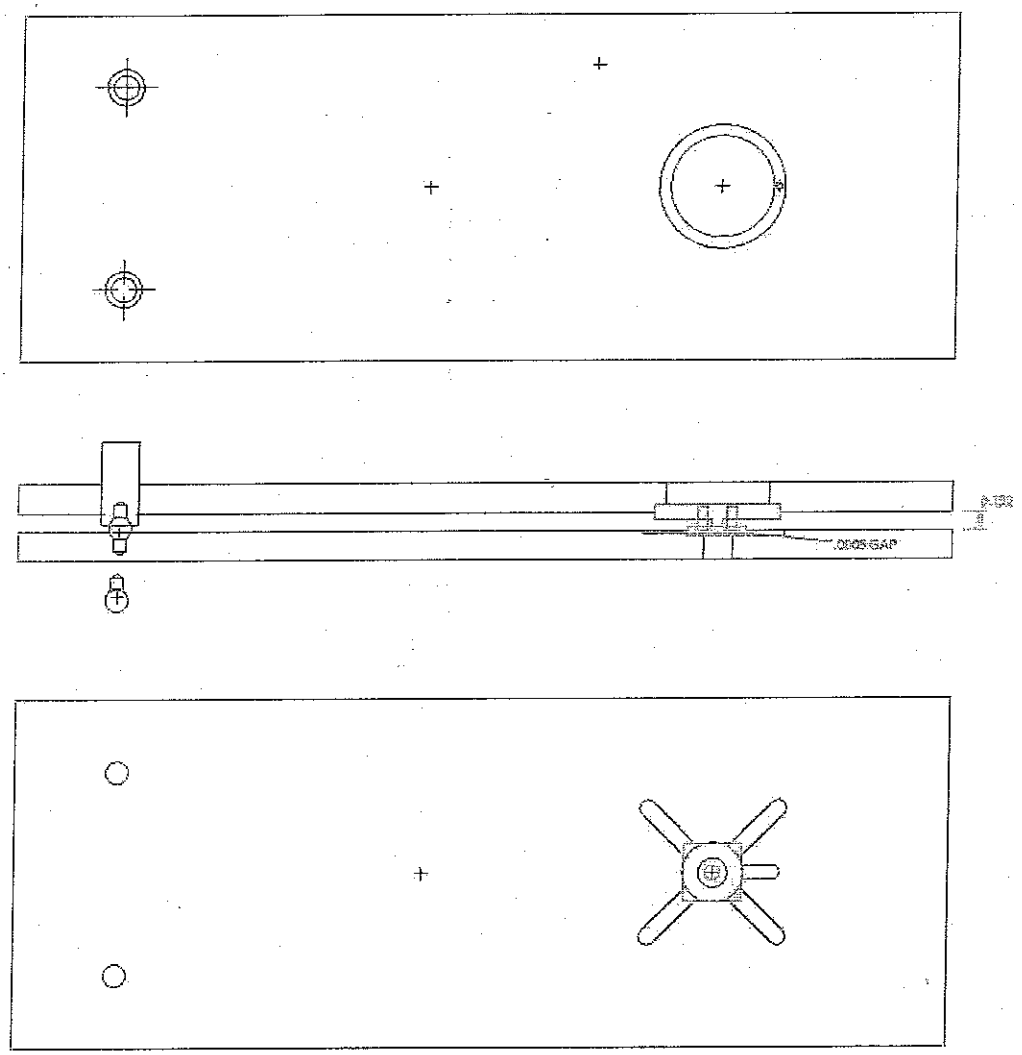

Figure A3. 3. Position of both jigs during the glueing process.

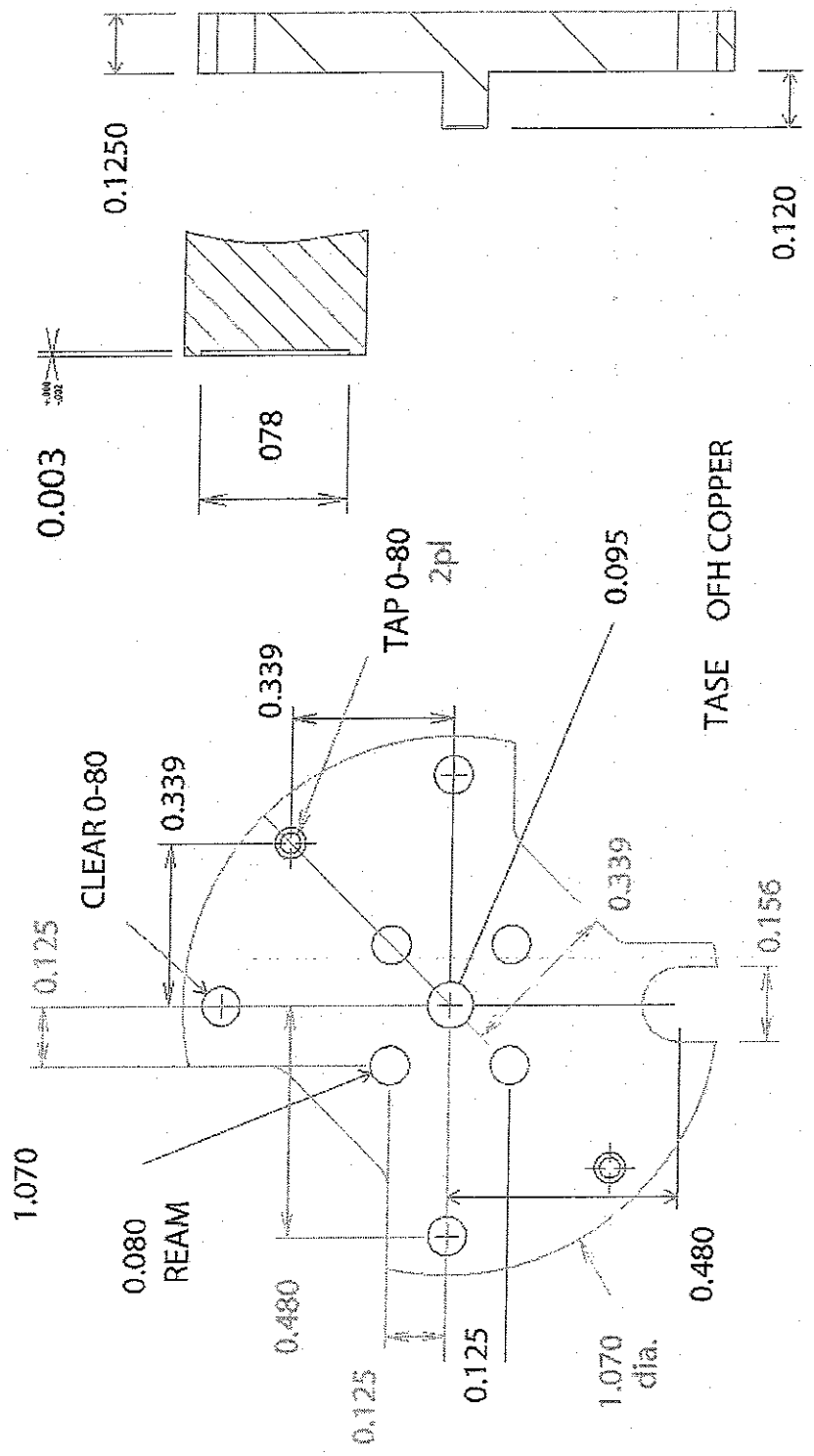

Figure A3. 4. A copper base with a central post blueprint.

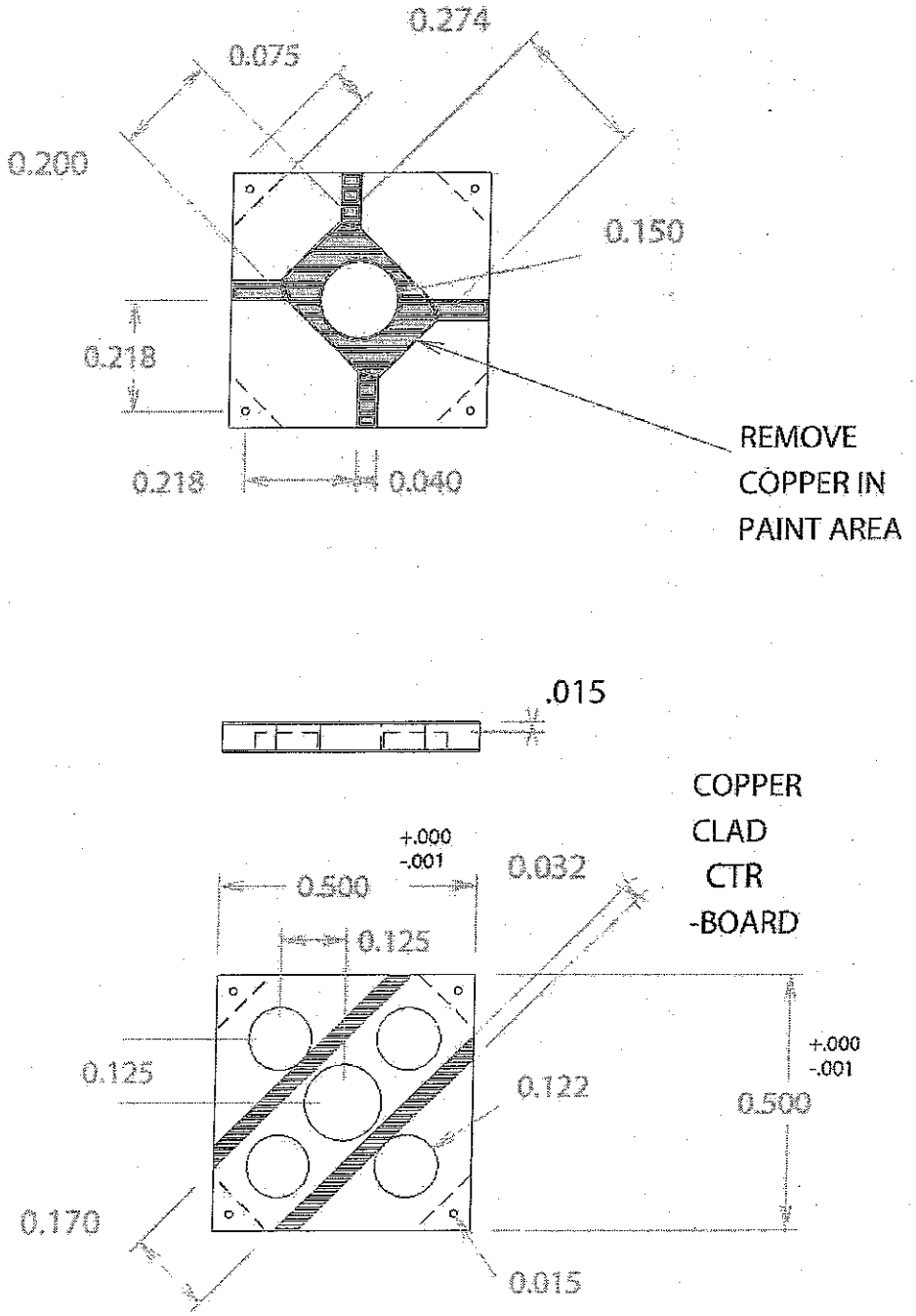

Figure A3. 5. Four transducers made of a circuit board.

▪ Appendix 4

To evaporate a sapphire disk on both sides including edges one needs to :

– *scratch central spot with a diamond scribe using 3 mm diameter mask;*

– *scrub with hands in gloves using alcanox soap;*

– *rinse with distiled water, then with methanol under nitrogen gas dry blow;*

– *assemble a rotor as depicted in the lab notebook;*

– *put slightly magic tape on a glass slide;*

– *glue a metal rod supported vertically to the tape over a weak spot;*

– *after glue hardens, cut the tape around metal rode perimeter;*

– *remove this rod from the slide;*

– *press gently over the scratched area of the sapphire disk;*

– *insert the rod into the rotator chuck inside the evaporation chamber;*

– *start rotating the disk before evaporating silver from each of two boats separately;*

– *achieve 2000 Å of silver thickness on each side of the sapphire disk.*

To glue sapphire disk to a central post of the copper base one needs to :

– *transfer sapphire disk by a rod into indent in the lower jig;*

– *turn on vacuum and detach the rod from the disk;*

– wipe a 12 μm thick plastic film with methanol and let it dry out;

– make four film spacing strips and lay them down diagonally in appropriate indents in the lower jig to cover the disk slightly near the edges;

– accurately center a capacitor plate (circuit bord square) in the lower jig on the top of sapphire disk with the spacers;

– make sure that capacitor is not grounded;

– install the copper base in the upper jig upside down using four screws;

– after cleaning a central post with methanol and dry blow, prepare Conap Easypoxy – 45 mixture with silver flakes to be viscous, not pastey;

– put a tiny amount of glue mixture on four central segments of the central post without spilling over the rim around central post perimeter;

– insert the upper jig with a base into the lower one using a pivot joint and slowly lower the former until central post rests on sapphire disk;

– tighten both jigs with a bolt in a spring by hand lightly;

– clamp the vacuum hose and wait for the glue to set.

To glue a capacitor plate one needs to :

– make another glue mixture, Stycast 1266, without silver;

– rinse four copper pins in methanol, dry them out in nitrogen gas;

– apply a little drop of glue on a copper pin end and insert the pin into base hole to reach the hole on the bottom side of the circuit board;

– repeat this procedure for the other three copper pins;

– check that capacitor is still not grounded;

– load the pin pusher with a stable weight to press on pins evenly to glue them well;

– use a lamp to warm up the assembly for about 24 hours.

To mount the base into a cryostat one needs to :

– remove the pusher with a weight;

– holding the upper jig, loosen the bolt with a spring;

– raise the upper jig with the base, then mount the base on a turntable;

– remove gently all spacers from the capacitor;

– check an electrical ground of all four transducers;

– cover sapphire disk with a dust cap;

– mount heater ring in a cell chamber;

– mount the base into a cell chamber;

– prepare the indium o-ring on a cell chamber flange;

– attach the drive and pick-up wires;

– remove the dust cap from the disk;

– close up the cell chamber and check all electrical contacts.

References

Chapter 1

[1. 1] P. L. Kapitza, Nature **141**, 74 (1938).

[1. 2] J. F. Allen and A. D. Meisner, Nature **141**, 75 (1938).

[1. 3] F. London, Nature **141**, 643 (1938).

[1. 4] S. N. Bose, Z. Phyz. **26**, 178 (1924).

[1. 5] A. Einstein, Sitzber. Kgl. Preuss. Akad. Wiss., (1924), p. 261.

[1. 6] R. P. Feynman, Phys. Rev. **94**, 262 (1954).

[1. 7] L. D. Landau, J. Phys. USSR **5**, 71 (1941).

[1. 8] W. Greiner, L. Neise, H. Stoker, Thermodynamics and Statistical Mechanics (Springer – Verlag, N. Y., 1994).

[1. 9] R. A. Aziz et al., J. Chem. Phys. **70**, 4330 (1979).

[1. 10] W. E. Keller, Helium – 3 and Helium – 4 (Plenum, N. Y., 1989).

[1. 11] P. E. Sokol et al., in Momentum Distributions, R. N. Silver and P. E. Sokol, eds. (Plenum, N. Y., 1989).

[1. 12] C. T. Lane, Superfluid Physics (McGraw – Hill, N. Y., 1962).

[1. 13] V. F. Sears and E.C. Svensson, Phys. Rev. Lett. **43**, 2009 (1979).

[1. 14] H. N. Robkoff et al., Phys. Rev. Lett. **43**, 2006 (1979).

[1. 15] V. F. Sears et al., Phys. Rev. Lett. **49**, 279 (1982).

[1. 16] R. K. Pathria, Statistical Mechanics (Pergamon, Oxford, 1972).

[1. 17] B. K. Agarwal, M. Eisner, Statistical Mechanics (John Wiley, N. Y., 1988)

[1. 18] H. R. Glyde, Excitations in Liquid and Solid Helium
(Clarendon Press, Oxford, 1994).

[1.19] D. R. Tilley and J. Tilley, Superfluidity and Superconductivity
(Adam Hilger, Bristol and New York, 1990).

[1.20] K. R. Atkins, Liquid Helium (Cambridge University Press, London, 1959).

[1.21] H. A. Mook, Phys. Rev. Lett. **51**, 1454 (1983).

[1.22] L. J. Campbell, Phys. Rev. **B 27**, 1913 (1983).

[1.23] M. H. Kalos et al., Phys. Rev. **B 24**, 115 (1981).

[1. 24] P. M. Lam and M. L. Ristig, Phys. Rev. **B 20**, 1960 (1979).

[1. 25] L. D. Landau and E. M. Lifshitz, Statistical Physics, Part 2
(Pergamon, Oxford, 1980).

[1. 26] I. M. Khalatnikov, An Introduction to the Theory of Superfluidity
(W. A. Benjamin, Inc., N. Y., 1965).

[1. 27] E. L. Andronikashvili, ZhETF **16**, 780 (1946).

[1. 28] V. P. Peshkov, J. Phys. USSR. **10**, 380 (1946).

[1. 29] L. D. Landau, J. Phys. USSR. **11**, 91 (1947).

[1. 30] R. J. Donnelly et al., J. Low Temp. Phys. **44**, 471 (1981).

[1. 31] F. London, Superfluids (John Wiley, 1954).

[1. 32] P. W. Anderson, Quantum Fluids (North – Holland, Amsterdam, 1966)

[1. 33] B. D. Josephson, Phys. Lett. **1**, 251 (1962).

[1. 34] B. D. Josephson, Adv. Phys. **14**, 419 (1965).

[1. 35] R. P. Henkel et al., Phys. Rev. Lett. **23**, 1276 (1969).

▪ Chapter 2

[2. 1] A. Ishihara, Condensed Matter Physics (Oxford, N. Y., 1991).

[2. 2] K. R. Atkins, Phys. Rev. **113**, 962 (1959).

[2. 3] L.D. Landau and E. M. Lifshitz, Fluid Mechanics (Pergamon, London, 1959).

[2. 4] F. E. Relton, Applied Bessel Functions (Dover, 1965).

[2. 5] R. Baierlein, F. M. Ellis and H. Luo, J. Low Temp. Phys. **108**, 31 (1997).

[2. 6] J. Reppy, in Phase Transitions in Surface Films,
J. G. Dash and J. Ruvalds, eds. (Plenum, N. Y., 1980), p. 233.

[2. 7] A. F. G. Wyatt, J. Phys : Condensed Matter **8**, 9249 (1996).

[2. 8] S. A. Jerebets and F. M. Ellis, J. Low Temp. Phys. **121**, 321 (2000).

[2. 9] S. A. Jerebets and F. M. Ellis, Physica **B 284 – 288**, 133 (2000).

[2. 10] F. M. Ellis and H. Luo, Physica **B 169**, 521 (1991).

▪ Chapter 3

[3. 1] G. E. Andrews, R. Askey and R. Roy, Special Functions (Cambridge, 1999).

[3. 2] S. C. Bloch, Introdauction to Classical and Quantum Harmonic Oscillators
(John Wiley, 1997).

[3. 3] R. Baierlein, Thermal Physics (Cambridge, 1999).

[3. 4] I. Rudnick, in Quantum Fluids, N Wiser and D. J. Amit, eds.
(Gordon and Breach, 1970).

[3. 5] A. Kent, Experimental Low – Temperature Physics (AIP, 1993).

[3. 6] I. M. Khalatnikov, Zh. Eksp. Teor. Fiz. **22**, 687 (1952).

[3. 7] O. V. Lounasmaa, Experimental Principles and Methods Below 1 K (AP, 1974).

▪ Chapter 4

[4. 1] F. M. Ellis et al., Rev. Sci. Instrum. **52**, 1051 (1981).

[4. 2] H. Luo, Ph. D. Thesis, Wesleyan University (1992).

[4. 3] M. Gauthier and E. J. Varoquaux, Cryogenics **13**, 272 (1973).

▪ Chapter 5

[5. 1] M. Kubitzki, Mechanical Resonances of a Third Sound Resonator

(preprint, Wesleyan University, 2001).

[5. 2] B. Kusse, E. Westwig, Mathematical Physics (John Wiley, N. Y., 1998).